OBSERVATION OF $K^{*0}(2060)$ IN THE $\phi K\pi$ FINAL STATE PRODUCED IN PROTON-NUCLEI INTERACTIONS AT 400 GeV/C

by

Sergio Torres

Dissertation submitted to the Faculty of the

Virginia Polytechnic Institute and State University

in partial fulfillment of the requirements for the degree of

DOCTOR OF PHILOSOPHY

in

Physics

APPROVED:

W.P. Trower, Chairman

A. Abashian

J.R. Ficenec

L.D. Roper

R. Zaiten

January, 1985

Blacksburg, Virginia

11/8/85 MCR

OBSERVATION OF $K^{0*}(2060)$ IN THE $\phi K\pi$ FINAL STATE

PRODUCED IN PROTON-NUCLEI INTERACTIONS AT 400 GeV/C

by

Sergio Torres

Committee Chairman: W. Peter Trower

Physics Department

(ABSTRACT)

In 1982 Fermilab experiment E623 took data in a search for high-mass boson resonances which decay into one or two ϕ mesons produced in 400 GeV/c proton-nuclei interactions. A hardware trigger selected 3.6 million events with identified K^+K^- pairs. Here I report my study of events with $\phi K\pi$ in the final state and present the first evidence for $K^{0*}(2060)$ decaying into $\phi K\pi$ and $\phi K^{0*}(890)$.

ACKNOWLEDGEMENTS

High energy physics experiments are conducted by large groups of people with a variety of skills. Experiment E623 was no exception. Personally I would like to thank my advisor Peter Trower for the inordinate time and effort he spent with me on this thesis; for his discussion of topics related to the experiment; for his important analysis suggestions and careful readings of the manuscript, for our almost daily interaction; and for our seemingly endless discussions and help with the plots.

CONTENTS

CONTENTS (cont.)

TABLES

FIGURE CAPTIONS

INTRODUCTION

The "standard model" asserts all matter consists of quarks, leptons and the gauge bosons carriers of the electromagnetic, weak and strong interactions. There are six known leptons; three electrically charged (electron, muon and tau) and three neutral (neutrinos ν_e, ν_μ and ν_τ). All leptons interact weakly with other particles while the charged leptons also interact electromagnetically.

In quantum field theory forces between particles result from the exchanging of field quanta (e.g., for electrons the exchange of virtual photons). The idea of intermediary particles was first introduced by Yukawa [1] who postulated that a force's range is inversely proportional to the mass of the particle that mediates it. The infinite range of the Coulomb force implies a zero rest mass photon. This idea was later rigorously implemented in Quantum ElectroDynamics (QED) [2]. QED has yet to be confounded by experiment and provides the example upon which theories of the weak and the strong interactions draw.

The strong force, responsible for binding quarks inside a hadron, is explained by Quantum ChromoDynamics (QCD). These particles interact by virtue of their "color" charge through the exchange of massless gauge bosons called gluons which can form bound states or "glueballs" [3]. Color was proposed to make the quark model consistent with the Exclusion Principle and it adds an extra degree of freedom for hadrons, which are made up by quarks. A gluon carries a two-color charge, that of the emitting and absorbing particles and there are eight distinct kinds of

gluons in all. Since color is thought to be confined, quarks and gluons are only seen in agglomerations with no net color.

The weak force is responsible for a number of physical processes: nuclear and particle β-decay, neutrino induced reactions and so on. The electroweak theory unified the electromagnetic and the weak forces [4]. Here the photon and the intermediate vector bosons that mediate the weak force ($W^{\pm}$ and Z^{0}) belong to the same family. Crucial to this theory is the concept of spontaneous symmetry breaking [5] that provides a mechanism by which the $W^{\pm}$ and the Z^{0} acquire mass. This is renormalizable [6] and thus, calculations with it are free of divergences.

The quark hypothesis was put forward in 1964 independently by M. Gell-Mann and G. Zweig [7]. In Gell-Mann's version there were three quarks differentiated by a new quantum number called flavor; up (u), down (d) and strange (s). In the intervening decade two new flavors have been discovered, charm (c) [8] and beauty (b) [9] and an additional one, top (t), postulated. Quarks, which carry electric charges of $+\frac{2}{3}|e|$ and $-\frac{1}{3}|e|$, interact electromagnetically, weakly and strongly, but are not theoretically allowed to be seen in isolation. The search for fractional charge in accelerator experiments, cosmic rays and in matter has produced no compelling evidence that quarks are not exclusively confined to hadrons [10]. The additive quark model has been remarkably successful in reproducing the quantum numbers and masses of all mesons and baryons. In this simple non-relativistic model a meson is a bound quark-antiquark pair and a baryon is a quark triplet. Materialized

hadrons look like atoms, their quarks in a central Coulomb-like field.

From the three lightest quark flavors nine mesons of each spin and space (J^P) configuration can be constructed. The pseudoscalar meson (0^-) states are π^+, π^-, π^0, K^0, K^-, K^+, $\bar{K}^0$, η and η'. The vector mesons (1^-) states are ρ^+, ρ^-, ρ^0, K^{*0}, K^{-*}, K^{+*}, $\bar{K}^{0*}$, ω and ϕ. Similarly baryon multiplets of 8 and 10 elements can be built with these quark flavors: the $\frac{1}{2}^+$ octet n, p, Σ^+, Σ^0, Σ^-, Λ, Ξ^- and Ξ^0, and the $\frac{3}{2}^+$ observed decuplet Δ^-, Δ^0, Δ^+, Δ^{++}, Σ^{-*}, Σ^{0*}, Σ^{+*}, Ξ^{-*}, Ξ^{0*} and Ω^-.

The neutral kaon, a down (d) and an antistrange ($\bar{s}$) quark in the ground state ($^1S_0$), has a mass of 494 MeV/c^2. Its observed excitations $K^{*0}(890)$ ($^3S_0$), $K^{*0}(1430)$ ($^3P_2$), $K^{*0}(1780)$ ($^3D_3$) and $K^{*0}(2060)$ ($^3F_4$) [11] are plotted with spin versus mass-squared [12] in Fig. 1.1. Our observed $K^{*0}(2060)$ decays into $\phi K^+\pi^-$ $(\bar{s}s)(\bar{s}u)(\bar{u}d)$ and $\phi K^{*0}(890)$ or their charged conjugate as diagramed in Fig. 1.2. Our results and those from other experiments which see the $K^{*0}(2060)$ are summarized in Table 1.1 [13-17]. In Table 1.2 are listed all $\phi K\pi s$ final states in which we might observe the $K^{*0}(2060)$ without neutral particle identification. Phase space and the restricted kaon momentum region permitted by the trigger (see Sect. 5.3) only allow us to see two of these states.

Fermilab experiment E623 was the second for the Arizona/Fermilab/Florida State/Notre Dame/Tufts/Vanderbilt/Virginia Tech collaboration. In the first, E580, we studied the $K^0_S\bar{K}^0_S$, $K^0_S\Lambda$, and $\Lambda\bar{\Lambda}$ final states [18,19]. E623 used the Fermilab Multiparticle Spectrometer (FMPS) in the M6W Meson Laboratory beam line with 400 GeV/c protons interacting with the nuclei of a segmented scintillator target. The

events were selected by a fast trigger processor programmed to identify at least two K^+K^- pairs whose effective mass in the magnet bend-plane was compatible with that of the ϕ. Experiment E623 was designed to study high-mass states which decayed into ϕ-mesons, such as glueballs and the η_c (a charm quark-antiquark). The $\phi\phi$ decay mode selects $(q\bar{q})_{c=+1}$ states which are not directly accessible to e^+e^- experiments because in these the hadrons are produced by the annihilation of the electron and positron and the subsequent creation of a quark-antiquark pair. The virtual particle is a photon (c=-1). In addition, if this state decays by an OZI [20] allowed channel (e.g., a decay in which the quarks of the decaying particle are present in the final state), it would select mesons having exotic structure, such as hadrons made up of more than three quarks.

The $\phi\pi$ [21] and $\phi\phi$ [22] final states from E623 have been analyzed elsewhere. I report here my study of the $\phi K\pi$ final state in which I have observed for the first time $K^{*0}(2060)$ decaying into $\phi K\pi$ and $\phi K^{*0}(890)$.

In Chapters 2 and 3 I describe the E623 detector and data acquisition procedure. I briefly discuss the off-line analysis in Chapter 4. In Chapter 5 I detail the properties of the $\phi K\pi$ system, present the $K^{*0}(2060)$ analysis and discuss error sources (e.g., particle identification inefficiencies and mass resolution inadequacies).

DETECTOR DESCRIPTION

2.1 General: A plan view of the FMPS located in the Meson Laboratory is seen in Fig. 2.1.1. The 400 GeV/c protons from the M6W beam were tracked in three proportional wire chamber (PWC) modules (BA1, BA2 and BB) located upstream 30 m, 10 m and 2.1 m, respectively, from the segmented scintillator target (S_T). Each counter presented a 3.2 × 3.2 cm^2 area to the beam, was 0.62 cm thick, was wrapped in aluminum foil and made light-tight with black tape. Material in the target produced ~ 0.2 inelastic interactions/beam-particle. A light pipe connected each counter to a RCA4517 photomultiplier tube (PMT) constructed with a bi-alkali photocathode whose sensitivity peaked at ~400 nm matching the Pilot-B scintillator (1.031 g/cm^3) emission spectra and light pipe transmissivity.

The superconducting ferrite magnet, 122 × 80 cm^2 aperture, produced a 16.9 kG centrally homogenous magnetic field at maximum excitation of 180 A. All charged particles moving along the beam axis experienced a change in momentum transverse to their direction ΔP_T=697 MeV/c. The superconducting magnet coil was wound so that the magnetic field direction was vertical and the bend-plane horizontal. For a singly charged particle (q=±1) with momentum P entering the magnetic field parallel to the beam, the deflection angle α is = $q\Delta P_T/P$, and the momentum resolution $\delta P/P = |\delta\alpha/\alpha| = P\delta\alpha/\Delta P_T$. At low momentum multiple scattering limits the precision with which the track direction can be determined. Thus, the momentum resolution becomes $\delta P/P$ =

$(P\delta\alpha/\Delta P_T)\sqrt{1 + (P_o/P)^2}$. With our chamber arrangement $\delta\alpha = 6.27\times10^{-4}$ and $P_o = 35$ GeV/c (see Sect. 5.1).

The upstream spectrometer arm had 5,312 wires in 15 planes in modules A, B and C centered at distances of 0.5, 1.05 and 2.16 m from the target, respectively. The downstream tracking (7,168 wires) was done in 10 PWC planes, the D and F modules centered at 4.8 and 8.9 m from the target, and 8 drift chamber planes, the DA and DB modules centered at 7.72 m and 8.47 m from the target respectively.

Two multicell threshold Cherenkov counters were used, C_B for particle identification and C_A as a general multiplicity detector for particles above threshold. A scintillator wall (S_W), seen in Fig. 2.1.2, was segmented to provide vertical position information in the center region where the particle density was largest.

2.2. Tracking Chambers: A multiwire PWC [23] is a plane of parallel equally spaced anode sense wires symmetrically positioned between cathode high-voltage planes. Electrons produced in charged particle interactions with the filling gas are accelerated by the electric field and cause avalanches just outside the space charge region near the anode wires. The resulting pulse is then amplified and recorded while the wire location gives position information where accuracy depends solely on the wire spacing: 0.6 mm and 0.3 mm for 2 mm and 1 mm wire spacing respectively.

The A station had 1536 wires in 6 planes oriented vertically (2), horizontally (2) and rotated at ±45° (1 each). The anode wires, 10 μm gold-plated tungsten, were spaced by 1 mm as were the cathode wires,

50 μm beryllium copper. The gas, argon with isobutane (.2) and Freon 13B1 (.005), was the well-known "magic gas" [23]. The assembled module was closed with 0.05 mm Mylar windows.

The B and C modules were constructed with 2 mm wire spacing. The C station limited the aperture upstream ($\pm 2.6 \times \pm 4.0$) mr^2 and receded in the magnet aperture. A thru F were PWCs whose characteristics are seen in Fig. 2.1.1, and all but the beam chambers and A station used a CO_2 (.17) and argon (.83) gas mixture.

The position sensitive drift chambers offered somewhat better spatial resolution than PWCs, typically ~0.3-0.6 mm. The drift chamber spatial resolution, which depends on the resolving time of the electronics (~2 ns), cell-to-cell constancy of drift velocity, and the known wire locations, was typically ~0.3-0.4 mm. A drift cell consisted of a sense wire held at ground potential and a thick field shaping anode that intensified the electric field in the low-field regions between sense wires.

A plane whose wires are vertical (horizontal) defines the x (y) coordinate. Similarly, rotated planes define the u and v coordinates. The DA and DB drift chamber modules each had 736 wires distributed in 4 planes oriented horizontally (1) and staggered (1), which resolved the ambiguity in assigning the track position with respect to a sense wire (the left-right ambiguity), and rotated by an angle $\theta = \pm \tan^{-1} 0.3$ (1 each).

The 1,472 sense wires signals were fed to amplifiers through balanced pair lines, and then to time-to-digital converters (TDCs) which

clocked the interval between the pulse arrival and a common stop time, defined by a delayed signal from the incident beam particle. Our TDC, LeCroy 4291B, had 32 channels in a single width CAMAC module each with 9-bits plus overflow for a 512 ns dynamic range and 3.6 μs conversion time with 1 ns least count. Some of the drift chamber characteristics appear in Table 2.2.1.

Sense wire pulses, ~ 1 μA amplitude and ~ 200 ns duration, measured electron drift time in the drift cell electric field. Electrons produced by ionization drift against the electric field with velocity v(t), and reach the sense wire where avalanche multiplication occurs at time t producing a signal that starts the clock for that channel. At some later time all channels are given the common stop signal (t_0). The track position with respect to the anode wire is $x = f(t_0-t) = \int_t^{t_0} v(t')\,dt'$.

The value of t_0 and the function f were determined from data; 1,472 TDC histograms were plotted. The t_0 was the distribution cut-off while the functional dependence on time was obtained by a 4th-order polynomial fit to the integral TDC spectra. This position information was known only with respect to the track-wire separation and not in direction, the left-right ambiguity. Using the nominal drift velocity of 50μm/ns for argon-ethane and the drift cell size of 1.905 cm, the modules could resolve up to 2.6×10^5 tracks/s.

2.3 Cherenkov Counters: The Cherenkov counter, C_A with 40 cells and C_B with 30, seen in Fig. 2.3.1, were to provide particle identification for the trigger processor on-line and for event selection off-line. C_A

actually only provided an on-line multiplicity veto.

C_B, whose characteristics are summarized in Table 2.3.1, consisted of a nearly planar array of individually positioned spherical mirrors enclosed in an atmospheric nitrogen filled box. The spherical mirrors were aluminized and overcoated with magnesium fluoride to assure reflectivity for ultraviolet Cherenkov light. The mirrors focused most of the light into similarly prepared Winston cones. We aligned the mirrors with a laser equiped theodolite located at our target, 5.6 m from the mirror plane. By tracing the perimeter and central cross of each mirror while adjusting its orientation until the maximum light entered its cone we, for most mirrors, focused this light directly on the PMT face.

Two different PMTs were used, 2" EMI9839KB for C_A cells and the 10 central C_B cells and 5" RCA8854 for the side cells. Since our PMTs were ultraviolet inefficient (75%) and the Cherenkov spectral distribution for nitrogen is ~70% in the ultraviolet, we coated each tube face with a layer of p-terphenyl wave-shifter which absorbed ultraviolet and reemited visible (520 nm) light, improving our detection efficiency defined by $\varepsilon=\varepsilon_0[1-\exp(-N)]$ [24], by 5%. N is the average number of photoelectrons collected on the photocathode and the overall efficiency ε_0 (0.15) includes the PMTs quantum efficiency and the system optical efficiency.

The PMT anode output fed both an analog-to-digital converter (ADC) and a discriminator that provided the Cherenkov counter input to the trigger processor. The ADC was a 10-bit LeCroy 2249A (55 μs conversion

time), whose output was written to magnetic tape as part of the event record and so was available off-line for particle identification.

EVENT SELECTION

3.1 The Trigger: The diffracted beam from a target bombarded by a slow extracted beam from the Fermilab synchrotron delivered 4×10^6 400 GeV/c protons in 1 s spills every 10 s to our experiment. The average trigger rate was 80/s so, most of the dead time (40%) came from the reading event words (30%). A trigger rapidly (~150 ns) selected events using a fast hardware processor whose program recognized tracks and computed kinematic quantities [25].

We triggered on events with ϕ mesons by detecting charged kaons which gave a reconstructed mass ≤ 1020 MeV/c^2 for oppositely charged pairs using their bend-plane projected momentum and angles. The lack of Cherenkov light in C_B signaled a kaon.

Three scintillation counters S_1, S_2 and S_3, located in front of the target, defined the beam. Counter S_3 vetoed wide angle beam tracks while the beam passed through a hole in its center. A particle was accepted if $BM = S_1 \cdot S_2 \cdot \overline{S_3} \cdot BMGT$, where BMGT was the beam gate from the accelerator. An interacting beam particle was $IB = BM \cdot dE/dX \cdot \overline{1\times1}$, where 1×1 was the 1" by 1" scintillation counter located between drift stations DA and DB. If no more than five C_B cells had light and the window discriminated charged particle multiplicity was ≤ 15 in dE/dX, the processor was gated (enable, $E = IB \cdot \overline{C_B > 5} \cdot \overline{dE/dX > 15}$). The production angles, invariant masses (M_L,M_R) and transverse momenta (P_{TL},P_{TR}) of the leftmost and rightmost K^+K^- combination pairs were computed. The decay $\phi \rightarrow K^+K^-$ has a Q

- 32 MeV, the kaon opening angle was, $\lesssim 7°$ for 5.9 GeV/c kaons. For two ϕ mesons produced in the decay of a heavy meson ($\gtrsim 2.5$ GeV/c^2) the opening angle should be, $\gtrsim 10°$ for 15 GeV/c phis, therefore the two K^+K^- pairs should be well separated.

The dE/dX counter, the C_X and D_X PWC planes, the DA_X drift plane, the C_A and C_B Cherenkov counters and the S_W scintillator wall, as seen in Fig. 3.1.1, were used in the trigger. The PWC and drift planes (each segmented into 32 cells) formed a hodoscope and provided space information by summing C_X and D_X signals from adjacent wires with OR amplifiers and logically ORing drift chamber pre-amp logic level signals.

The anode signals from the C_A and C_B Cherenkov cells and the S_W scintillator wall were fed into a NIM discriminator that presented a logic level to latches activated with a trailing clock pulse edge (positive slope) applied to the front panel. Each hodoscope cell had a latch, thus, 190-bits were available to the trigger processor; $C_X(32)$, $D_X(32)$, $DA_X(32)$, $C_A(32)$, $C_B(30)$ and $S_W(32)$.

A track whose momentum was above the threshold for pions to produce light and below that for kaons was called a kaon when no Cherenkov signal was detected in the appropriate Cherenkov counter cell. A Monte Carlo program generated all allowed ($\bar{C}_B \cdot S_W \cdot DA_X$) track combinations.

To facilitate kaon identification the average particle multiplicity per event was limited. Since no light in the Cherenkov cell intercepted by a particle defined a kaon, a fast pion ($P_\pi > 5.7$ GeV/c^2) sharing a mirror with a kaon would show light and the kaon would be lost. For

each trigger element the multiplicity cuts were $C_x = (4,9)$, $D_x = (4,9)$, $DA_x = (4,10)$, $C_A \leq 7$, $C_B \leq 5$ and $S_W \leq 6$, where the limits (NL,NH) are defined as $NL \leq N \leq NH$. These cuts were used to form a gate, $EG = E \cdot C_x(4,9) \cdot D_x(4,9) \cdot DA_x(4,10) \cdot \overline{C_A > 8} \cdot \overline{C_B > 5} \cdot \overline{S_W > 7}$. Since the processor preferentially selected events where the Cherenkov counter C_B is inefficient, the C_B and C_A multiplicity were required to agree to within 2.

The inverse momentum was measured as the difference between where a particle struck DA_x and where it would have hit had it had infinite momentum. The 32 C_x bits for positive particles, were connected to the inputs of two priority encoders that selected K^+K^- pairs. The result was two 5-bit C_x hodoscope addresses whose values were proportional to the x-coordinate. The same was done for negative tracks. The left-most positive and negative kaons were selected as the left ϕ candidate. These 4 logical decisions ran in parallel for speed.

The ϕ opening angle was obtained by subtracting the two 5-bit C_x addresses. These five bits and the two 3-bit inverse momentum words went to a PROM/Multiplexer arranged as a 2048 × 1 memory. The PROMs had been programed using Monte Carlo results to favor low effective mass (≤ 1.02 GeV/c^2) K^+K^- pairs.

Each K^+K^- candidate pair was fed to its own P_T 256 × 4 PROM which was programed to provide four P_T bits for each kaon. The two 4-bit kaon-pair words were presented to a second 256 × 4 PROM which made the absolute word sum. This 4-bit result, whose range was 0 to 15, was compared with a DIP switch set threshold. The trigger definitions and

the typical trigger rates are shown in Table 3.1.1.

3.2 On-line Analysis: Trigger selected events were written to tape by a PDP11/45 computer operating under RT-11. The words were taken from an event buffer in CAMAC [26] modules which interfaced between the computer and the detector.

MULTI, the on-line data acquisition program, performed a series of operations on the data buffers. Globally, buffers were taken from a buffer-pool, filled with data from CAMAC, written to tape, given to the analysis and plotting routines and returned to the pool. The program provided for calls to user-written subroutines during event read-in. Diagnostic data were accumulated and displayed on demand throughout a run. These subroutines, for example, provided individual event displays, chamber hit distributions, and so on.

Our MULTI was arranged in blocks of 16 buffers, each 3,840 16-bit words long which accommodated ~ 6 events each up to 1,700 words long. The first 5 words of an event record were a header block that contained the byte count and the record type, 1 = data, 2 = between spills. Next were the 132 ADC words (S_T, dE/dX, C_A and C_B, and scalers), 14 trigger latch words, the drift chamber TDC block, and the PWC shift register block. The later consisted of a pointer to the PWC module and numbers of those wires that registered a signal.

DATA ANALYSIS

4.1 Track Reconstruction: The pattern recognition program used to analyze E623, FLOWERS, was written in FORTRAN for the VAX 11/780. The philosophy of this code was that computer time was more valuable than computer space. It read a physical data record, initialized for the first event and unpacked all the logical records in the physical record. The first event was setup and the scintillator target was analyzed. If there was no vertex, or too many vertices were found, the event was skipped. Beam information was used, when available, to find the x and y vertex coordinates one of which was passed to the pattern recognition subroutine.

The pattern recognition algorithm first found a track in the downstream x-z "view," since these tracks spread out more after passing through the magnet. Once the downstream view was processed, the upstream view where all tracks came from a single production vertex, was analyzed. Further, the trigger processor provided roads within which to search for kaons.

The found tracks in the downstream x-z view were extrapolated to the mid-magnet plane and then to the production vertex, while upstream hits were searched for along these extrapolated tracks. A three parameter fit was made to hits in the x-z plane, with the upstream and downstream portions constrained to intersect near the magnet midpoint.

Next the y-z projection was searched for tracks using only the rotated chambers, which could be transformed into y-coordinates by

$y=(u - x\cos\theta)/\sin\theta$, where the u-coordinate was rotated by the angle θ. Once the crude y-z projection was found the real y-coordinates were obtained and the track in y-z was refit now using both the y and rotated coordinate chambers. A 2 parameter fit to a straight line versus arc length was then made in the y-z view.

E623 generated 3.65×10^6 event triggers (runs 42-247). After pattern recognition 3.2×10^6 events remained. The cuts in this step required at least three particles in the event and at least one positive and one negative track with momenta between 5.0 and 25.0 GeV/c.

Next a global 3-dimensional 6 parameter fit was made to all the tracks of the 2.6×10^6 events that passed the cuts made by the fitter program, TIPTOE. The cuts were at least 3 fitted particles in each event with at least one positive and one negative kaon with momenta between 5.5 and 25.0 GeV/c. The possible kaons were determined by counting the fitted tracks with momentum between 5.5 and 25.0 GeV/c in each C_B cell. If there was no light then all the tracks were attributed to kaons. If there was light all but one was called a kaon unless a track with momentum greater than 25 GeV/c was present, then all were called kaons. Here kaons were assumed to have zero Cherenkov cone angle while pions were given a finite light cone so they could produce light in more than one cell.

Next the particle identification, described in Sect. 4.2, was made and a Data Summary Tape (DST) was produced consisting of 1.8×10^6 events. Here each event had at least 3 tracks with at least one positive and one negative kaon with $5.7 \leq P \leq 23.0$ GeV/c. There were

144,471 events with at least 2 positive and 2 negative kaons, the 4-K sample, which were written to 2 DST volumes.

4.2 Particle Identification: A charged particle moving through a transparent dielectric radiates a small amount of energy if its velocity is greater than the phase velocity, c/n, of light in that medium. This effect, first observed by Cherenkov [27] in 1934, was explained in 1937 by Tamm and Frank, using classical electrodynamics, who predicted that this radiation would be polarized, focused in a cone-shaped wave front and produced with a time constant of $\sim 10^{-11}$ s. The electric field vector polarization is in the particle-velocity and photon-momentum plane. The Cherenkov light cone angle for a particle moving at velocity fraction β in a refractive medium of index $n = 1 + \delta$ ($\delta << 1$ for a gas) is $\cos\theta = 1/n\beta$ or $\theta \approx \sqrt{2\delta - 1/\gamma^2}$, where $\gamma = p/m$. At $\theta = 0$ is the momentum threshold, P_{th}, at which the particle begins to produce light: $\gamma_{th} = 1/\sqrt{2\delta}$. The number of visible photons produced in a radiator of length R_ℓ cm is $N_p = 500\, R_\ell\, (1 - 1/\beta^2 n^2) \approx 1000\, R_\ell\, \delta\, [1-(\gamma_{th}/\gamma)^2]$. The photoelectron yield, normalized to N = 5 photoelectrons, with momentum is seen in Fig. 4.2.1.

The Cherenkov effect is used here to separate pions from kaons. Its threshold dependence defines 4 distinct momentum regions as seen in Fig. 4.2.2. In the first, charged particles below the pion momentum threshold (T_π) will not produce Cherenkov light, and thus could be a pion, kaon or proton (π/K/p low). Similarly, a momentum above T_π and below the kaon threshold (T_K) would be a pion if it produced light or ambiguously (K/p) if there was no light. In the third region a particle

momentum between T_K and the proton threshold (T_p) would be a proton if no light was detected and an ambiguous π/K if light was seen. Particles with momentum above T_p are ambiguously $\pi/K/p$. Because of their abundance (typically, for pp interactions at 400 GeV/c and $X_F \sim 0$, the ratios are $\pi/K \approx 8$, $\pi/\bar{K} \approx 20$, $\pi/p \approx 18$, and $\pi/\bar{p} \approx 100$ [28]) we resolve all ambiguities involving pions as pions. The region labeled 'e' is that of tracks with momentum below threshold for pions that gave light, they can be electrons. Finally in the region above threshold for protons, where all tracks should emit light, there is a small fraction (0.8%) of tracks which due to the inefficiency of the detector or spurious track finding are not possible to identify because no light was detected.

If there were fewer than 4 particles that could produce light in a Cherenkov cell we could determine if a given particle did produce light [29]. This was accomplished using both the ADC words and processor tagbits (C_B latches) written in the 132 word ADC block for each event buffer. Its proximity to the target and its location in the magnetic field made the C_A data ambiguous and unusable: 62% of C_A decisions disagreed with the more reliable C_B π/K identification.

The Cherenkov particle identification required knowing for each C_B cell the 1-photoelectron level, the efficiency and the pedestal level. The pedestals were determined from ADC words written between spills, corresponding to the pulse height with no particles present. The 1-photoelectron level, determined from the pulse height distributions for a sample of slow tracks (5.8 P 10.0 gev/c), was taken as the number of channels from the pedestal to the center of the first discernible

peak. For the central mirrors these distributions were random and their 1-photoelectron response was indeterminate. The above effect was seen because the AC coupling of the PMTs to the ADCs jammed at the high rate. Similarly, pulse height distributions for fast particles ($P \gtrsim 60$ GeV/c) were used to calculate individual efficiencies, $\epsilon = N/N_p$, where N was the most probable (excluding pedestal tail) number of photoelectrons and N_p, the number of photons ($350 \lesssim \lambda \lesssim 700$ nm) produced in a radiator with $R_\ell = 177$ cm and $n = 1.0003$, $N_p = 71[1-(\gamma_{th}/\gamma)^2]$, or ~70 for a $\beta=1$ particle. The individual cell efficiencies were ~10% for the central mirrors and ~6% for the side mirrors. This overall efficiency was [24] $\epsilon = [1-\exp(-N)] \times$ (PMT quantum eff.) $\times$ (radiator losses) $\times$ (reflection losses) $\times$ (PMT window and wave shifter losses), where the quantum efficiency was the average number of photoelectrons emitted from a photocathode per incident photon of a given wavelength, typically ~ 25%, and N, the average number of photoelectrons collected in the photocathode, was N ~ 5.

The AC coupling of the PMTs to the ADCs produced deadtimes in the ADCs that caused zero Cherenkov readings. Other inefficiencies were produced when the ADCs failed to reset, then an overflow count was registered. Table 4.2.1 summarizes our operational Cherenkov experience for each of the cells in C_B.

4.3 Identification Algorithm: The E623 particle identification algorithm used the projected Cherenkov cone area on the mirror plane, approximated as a circle whose radius was calculated to account for the radiation distribution on the mirror surface which is inversely

proportional to the distance from the circle center. The expected number of photoelectrons in each mirror was calculated by summing the contributions of each track to each mirror. The radius of the projected circle -cone radius-, $R = R_\ell \sin\theta$, where R_ℓ was the radiator length, in terms of mass and momentum is $R = R_\ell [1-(1+m^2/p^2)n^{-2}]^{1/2} = R_\ell\theta = R_\ell\sqrt{2\delta[1-(\gamma_{th}/\gamma)^2]}$. The number of expected PMT photoelectrons (N_e) is proportional to the number of photons emitted in the radiator (N_p) and the detector efficiency (ε) as $N_e = \varepsilon R_\ell \sin^2\theta$. This may be recast in terms of the particle mass and momentum as well as the number of photoelectrons (N) for $\beta = 1$ as, $N_e = N [1 - (\gamma_{th}/\gamma)^2]$. The particle mass was unknown so first the expected number of photoelectrons was calculated assuming a pion, then as a kaon, and finally as a proton.

The expected number of photoelectrons was stored by mirror number, which we loop over in ascending order of number of tracks that hit the cell; first looking at cells with one track, then two, and so on. The calculated pulse height for each mirror was $P_j = (ADC_j - PED_j)/L_j$, where ADC_j, PED_j and L_j are for the jth mirror ADC, pedestal and one-photoelectron respectively.

For cells with pulse height below the one-photoelectron level we looked at the cell tagbit and assigned a mass to tracks that had $\geq 30\%$ of its weighted area inside the mirror. Only a small fraction ($\sim 9\%$) of the time the tagbit information was in disagreement with the ADC readings. We calculated the mass according to the particle momentum and stored this information in the ID array.

Next we looped over mirrors with signals above the one-photoelectron

level and accounted for the signal. We first took fast tracks ($P \geq T_p$) and since they should give light we subtracted the corresponding signal from this channel. Assuming the particles to be pions, kaons and protons, we assigned the identification that yielded a result closest to zero after subtracting the calculated yield from the theoretical value. If light remained we took particles above kaon threshold and repeated the procedure. Failing that, we did the same as for particles above pion threshold. If no more light remained, the other particles were resolved according to the momentum region in which they fell. Otherwise decided by comparing with the theoretical value.

We calculated a weight that indicated the degree of isolation of each particle defined as, $W_j = 99/A$, where A was the sum of the areas, weighted by 1/R, of the circles, or fractions thereof, that went through the mirror. For example, a weight of 33 indicated that together with the particle there were 2 additional particles in the cell. Two or more particles in a cell with no light would have a weight of 99 each. The normalization to 99 resulted for representing the weight by 2 digits. Table 4.3.1 summarizes the multiplicities for each charge and momentum region for the 144,471 events in the 4-K sample.

An absolute determination of the overall pion-kaon separation efficiency was not possible, since we didn't have a "tunable" source of kaons and/or pions to calibrate the apparatus. However we estimated the contamination level in the pion and kaon samples by counting $\pi\pi$ combinations in a mass spectrum where a $K^{*0}(890)$ would appear if a kaon was misidentified as a pion. This could happen when a kaon shared a

cell with another track whose momentum was above threshold for Cherenkov emission. This $K^{*0}(890)$ peak would be seen at 620 MeV/c^2 as determined by Monte Carlo. For this test only pions from the π region of Fig. 4.2.2 were used. The resulting 46 misidentified $K^{*0}(890)$ combinations, determined by a fit to the $\pi\pi$ spectrum, seen in Fig. 4.3.1, represents a 13 % of the total $K^{*}(890)$ sample (305 events from the fit to the $K\pi$ mass spectrum and these 46 events).

THE $\phi K\pi$ SYSTEM

5.1 Single ϕ production: E623 was designed to look for double ϕ events and we collected 144,471 events with at least 2 K^+s and 2 K^-s, the 4K sample. Of these, 32,044 events had at least 1 K^+K^- mass combination within ± 6 MeV/c^2 of the nominal ϕ mass, 1020 MeV/c^2. Those with at least 1 $(K\pi)^0$ in addition to the ϕ were 25,482. The analysis that follows (except the $\phi K\pi$ mass spectrum in Fig. 5.2.1) is based on this sample of events only. The following cuts were made on the basis of reducing the backgrounds: (a) Only tracks that pass the fitter quality tests were used, (b) In the y-z view there were tracks that shared the same track points in this view (duplicate tracks). To resolve the ambiguity, if the opening angle in the y-z view of two tracks was less than 0.3 mrad the track with the least number of hits was excluded. (c) The reconstructed vertex must be within 3σ from the known target limits, and (d) tracks that do not produce a signal in the corresponding scintillator wall (S_W) segment were excluded.

Inclusive $\phi(s\bar{s})$ production has been studied previously [30]. We take advantage of the large $\phi \rightarrow K^+K^-$ branching fraction (.49) to look for ϕs. Kaons were defined as particles with $5.8 \leq P < 20$ MeV/c which did not produce light in Cherenkov counter C_B. Pions were particles with $P > 5.8$ GeV/c that gave a C_B signal, and included tracks from the π, π/K, and π/K/p high regions of Fig. 4.2.2.

For all fits in table 5.1.1. the background functional representation used was a polynomial of the form $N(M-M_0)^{\alpha}\exp[-\beta(M-M_0)]$.

N is an arbitrary normalization factor. The threshold-like mass (M_0), α and β were free to vary in the fit and their numerical value is listed in table 5.1.1. The function is arbitrary and was chosen because with few parameters it gives the best goodness of fit when compared with fits using other polynomials. For the resonances a Gaussian was used in the K^+K^- and $K\pi$ cases since the resonance widths were comparable to our mass resolution; a s-wave Breit-Wigner convoluted with a Gaussian resolution function was used for the $\phi K\pi$ fits. The fitted functions are superimposed on the histograms only in the range where the fit was done.

A fit to the K^+K^- mass distribution for $pN \rightarrow K^+K^-K^+K^-X$ events, seen in Fig. 5.1.1, gave 3,787±199 ϕK^+K^- events above background. The fitted mass and width (FWHM), 1019.6±0.3 and 9.6±0.6 MeV/c^2, are consistent with the accepted values [11] (1019.5±0.1 and 4.22±0.13 MeV/c^2) given our Monte Carlo determined ~8 MeV/c^2 (FWHM) resolution at the ϕ mass ($9 - \sqrt{8^2 + 4.2^2}$).

Two momentum dependent effects dominate our mass resolution. For slow particles it was multiple Coulomb scattering while for high momentum particles it was angular resolution upstream of the magnet. Thus, we parameterized the single charged particle momentum resolution using the expression introduced in section 2.1, as $\sigma_p/P = (P/\Delta P_T)\ \delta\alpha\ \sqrt{1 + (P_0/P)^2}$, where ΔP_T is the momentum kick given to the particle by the magnetic field and $\delta\alpha$ depends on the measured production angle uncertainty and includes the angular resolution before and after the magnet, the latter being smaller. At momentum P_0 the multiple scattering uncertainty equals the angular resolution. The two

parameters were estimated using 20,000 Monte Carlo generated $D \rightarrow \phi\pi$ events assuming δ-function masses for the D(1865) and $\phi(1020)$ mesons. These events were propagated through the FMPS computer codes that takes into account the detector geometry and the trigger processor cuts. The momentum vector magnitude was wiggled by a normally distributed δp, where $p \rightarrow p + \delta p$. The quantities $\delta\alpha$ and P_0 were adjusted to get D(1865) [21] and $\phi(1020)$ FWHMs consistent with those of the fitted data. The values for $\delta\alpha = 6.27 \times 10^{-4}$ and $P_0 = 35$ GeV/c corresponded to measured production angular uncertainties of $d\theta_x \sim d\theta_y \sim 0.44$ mr and 0.5 radiation lengths of material.

The angular resolution was limited by the short upstream lever arm. The 2.86 m between the A and C chambers and their 1 mm (2 mm for C) wire spacing gives $d\theta_x = \delta x/L \sim 0.3$ mr. Material in the scintillator target, chamber windows and the C_A Cherenkov counter (0.7 cm of glass, 6.2 cm of scintillator and 0.3 cm of Mylar) accounts for the multiple scattering. The result of this calculation is a resolution (FWHM) of 25±15 MeV/c^2 for $\phi K\pi$ at 2060 MeV/c^2 and 20±12 MeV/c^2 for $K\pi$ at 890 MeV/c^2.

Systematic errors in the mass scale would be produced by errors in the angular scale or momentum scale. For example, inaccurate knowledge of the magnetic field. To estimate this effect on the $K^{*0}(2060)$ we scaled the ϕ decay kaon momenta by a small fraction (0.04) until the fit to the ϕ mass became unacceptable (5σ from the nominal value). The corresponding mass shift in the $K^{*0}(2060) \rightarrow \phi K\pi$ when the momenta of all the decay tracks are scaled by 0.04 was 17 MeV/c^2, or 0.8%.

5.2 Observation of $K^{*0}(2060)$: The $\phi K\pi$ mass spectrum shown in Fig.

5.2.1 includes low momentum tracks ($P \leq 5.8$ GeV/c) and weak enhancements around 2 GeV/c^2 are seen. To reduce the background only identifiable tracks ($P > 5.8$ GeV/c) were used and those tracks that failed to produce a signal in the scintillator wall S_W were excluded from the event. This cut left us with the sample of 25,482 $\phi(K\pi)^0X$ events used in the analysis whose results are reported in this thesis. The $\phi K\pi$ mass spectrum, seen in Fig. 5.2.2, shows an enhancement whose fitted mass and width are 2079±7 and 61±58 MeV/c^2. For this fit a Breit-Wigner of central value M_0 and full width Γ_{BW} at half maximum convoluted with a Gaussian resolution function ($\sigma = 10$ MeV/c^2) was used. The resulting measured distribution is:

$$g(x') = y\sqrt{\pi}\ \mathrm{Re}[w(z)]$$

where,

$$w(z) = e^{-z^2}\left(1 + \frac{2i}{\sqrt{\pi}} \int_0^z e^{t^2}\, dt\right) ,$$

$$z = x + iy, \quad x = (x' - M_0)/\sigma\sqrt{2}, \quad y = \Gamma_{BW}\sigma\sqrt{2M_0} .$$

Measured widths range from 52±50 to 540±300 MeV/c^2 [13-17]. The fit gives 431±116 events above a background whose parameters are shown in table 5.1.1. The $\phi K\pi$ background, seen in Fig. 5.2.3, was constructed from K^+K^- pairs whose mass is in the side-bands outside the ϕ mass-band ($1002 \leq M < 1014$ and $1026 \leq M < 1038$ MeV/c^2) and is roughly the same as Fig. 5.2.2 except the $K^*(2060)$ signal is absent. The separate $\phi K^+\pi^+$ and $\phi K^-\pi^-$ distributions, seen in Fig. 5.2.4, show no structure, ruling out isospin of $\geq 3/2$ as expected for a K^* resonance.

The transverse (P_T^2) and longitudinal (X_F) momentum distributions corrected for acceptance, are seen in Figs. 5.2.5-6. $X_F = P_\ell/P_\ell^{max} \sim 2P_\ell/\sqrt{s}$ was introduced [31] as a scaling variable for inclusive hadronic interactions at large energies. P_ℓ is the center-of-mass momentum along the beam direction while P_ℓ^{max} is its maximum and $\sqrt{s}$ is the total interaction energy in the center-of-mass.

The background for the X_F and P_T^2 plots was obtained from mass side-bands in the $\phi K\pi$ system [72 MeV/c^2 above and below that of the $K^{*0}(2060)$] and when subtracted left 347 events in the signal. Since our experiment was designed to study central production, we have narrow X_F distributions centered at zero and therefore can say little about the X_F dependence of final states. Further, the narrow momentum range in which our detector can identify kaons limits our sensitivity to $|X_F| \leq 0.1$. The P_T^2 distribution was fitted to $\exp(-bP_T^2)$ giving $b = 2.3\pm0.7$ (c/GeV)^2 consistent with that from other K^* resonances [19,32].

5.3 <u>$K^{*0}(2060)$ Decay Modes</u>: The mass spectra for the possible decay modes listed in Table 1.2 are shown in Figs. 5.3.2-6. The $K^{*0}(2060)$ is only seen here in $\phi K\pi$ and $\phi K^{0*}(890)$ states. The $K\pi$ mode is not seen mainly because the poor mass resolution (120 MeV/c^2) at 2.07 GeV/c^2, the large Q of this decay, 1446 MeV/c^2, produces kaons outside the momentum accepted in our trigger, and since it yielded only 2 charged kaons it would not satisfy the trigger. To see how large this effect and other effects (geometric acceptance, particle identification inefficiencies, etc) are, $K^{*0}(2060)KKKX$ events were generated with a differential cross section proportional to $(1-|X_F|)^{2.8}\exp(-2.5P_T^2)$ [19,32], where P_T and X_F

are the momentum transverse to the beam and the Feynman X of the generated $K^*(2060)$. A Monte Carlo program that takes into account the geometry of the magnet, the proportional wire chambers and the drift chambers, the momentum window of the Cherenkov counters, the particle identification inefficiencies due to overlapping of more than two Cherenkov light cones in the same cell, multiple scattering effects and the trigger processor was used to propagate the generated $K^*(2060)$ events. The acceptance is defined as the ratio of events surviving all cuts to the number of events generated. As we mentioned above, the $K\pi$ decay mode of the $K^*(2060)$ had little chance of being seen given our acceptance: the results of the Monte Carlo program indicated that only 4% of the kaons coming from the decay of the $K^*(2060) \rightarrow K\pi$ fall in the momentum window of the Cherenkov counter ($5.8 \leq P < 20.0$ GeV/c) for pion kaon separation, and the acceptance for this decay mode is 0.01%. Assuming a cross section for $K^*(2060)$ production of 22 μb as given by the Bourquin-Gaillard phenomenological model [33] extrapolated to our center of mass energy ($\sqrt{s} \approx 27$ GeV/c^2) and explained in section 5.7 of this thesis, and using the measured [15] branching ratio $B[K^*(2060) \rightarrow K\pi] = 0.07 \pm 0.01$, the upper limit on the number of events one would expect to see in this experiment is calculated to be 122 ± 64 events, which is not incompatible with the 23 ± 53 events as determined from the fit to the $K\pi$ mass spectrum seen in Fig. 5.3.1. For the above calculation, use was made of the definition of cross section: $\sigma = N_0 S/A$, where N_0 is the number of observed events, S is the sensitivity or nanobarn equivalent of the experiment and A is the acceptance. These

variables are explained in more detail in section 5.7 of this thesis.

The higher multiplicity multi-pion states are very close to threshold and hence phase space reduces their branching fraction for decay. For instance, consider the decay of a particle of mass M and momentum P into n daughters ($M \rightarrow m_1 + m_2 + \ldots + m_n$). The partial decay rate $d\Gamma$ in the rest frame of M is [34]:

$$d\Gamma = \frac{(2\pi)^4}{2M} \; |T|^2 \; \delta^4(P - \sum_{i=1}^{n} p_i) \; \prod_i \frac{d^3p_i}{(2\pi)^3 \; 2E_i}$$

T is the Lorentz invariant matrix element and the δ function takes care of energy-momentum conservation. It is seen from the above expression that for each additional particle in the final state a suppression factor proportional to the volume in phase space times $1/8\pi^3$ multiplies the decay rate. For example assuming that the dominant suppression comes from the $1/8\pi^3$ factor, the ratio $R = \Gamma[K^*(2060) \rightarrow \phi K\pi\pi]/\Gamma[K^*(2060) \rightarrow \phi K\pi]$ is $< \kappa/8\pi^3$, where κ includes the acceptance ratio $A(\rightarrow \phi K\pi)/A(\rightarrow \phi K\pi\pi)$ and the phase space volume factor ($\kappa < 1$). The acceptance calculation was done for each one of the decay modes using the Monte Carlo technique as described above for the $K\pi$ decay mode. Assuming a $1/8\pi^3$ suppression factor for each additional pion in the final state and using the acceptance given by the Monte Carlo program, an upper limit to the number of events for each mode is calculated. Table 1.2 summarizes this results. For these decay modes all tracks with momentum ≤ 5.8 GeV/c^2 were defined as pions and included in the event, otherwise the acceptance would be too small ($< 1.6\times10^{-5}$).

Since the $K^*(2060)$ is an isospin $\frac{1}{2}$ particle one would expect to see both the charged and neutral members of the iso-doublet. The neutral $K^*(2060)$ is seen in the $\phi K^{\pm}\pi^{\mp}$ and $\phi K^{*0}(890)$, and the corresponding charged modes are the $\phi K^{\pm}\pi^0$, $\phi K^0\pi^{\pm}$ and $\phi K^{\pm *}(890)$ which we can not study because our detectors were not designed for neutral particle detection. Thus we looked for the charged $K^*(2060)$ in the $\phi K^{\pm}$ channel but no apparent enhancement around 2.06 GeV/c^2 was visible (see Figure 5.3.2). However a total of 35±58 events was determined from the fit to the spectrum in Fig. 5.3.2.

To investigate the $K^{*0}(2060)$ decaying into $\phi K^{*0}(890)$ with $K^{*0}(890) \rightarrow K\pi$, we first looked at the $K\pi$ mass spectrum, seen in Fig. 5.3.1, for $K^{*0}(890)$ whose fit (see table 5.1.1) gave a 305±91 event excess in the sample of 25,482 $\phi(K\pi)^0X$ events.

To see $K^{*0}(2060)$ in the $\phi K^{*0}(890)$ channel we plot the $\phi K\pi$ mass spectrum for $K\pi$ mass combinations within ±40 MeV/c^2 of the $K^{*0}(890)$, seen in Fig. 5.3.8.a. The $K^{*0}(2060)$ is clear and a fit to a Breit-Wigner convoluted with a Gaussian resolution function gives 166±46 events above background. The $\phi K\pi$ mass spectra, seen in Fig. 5.3.8.b, for $K\pi$ mass combinations outside the $K^{*0}(890)$ mass-band ($770 \leq M(K\pi) < 850$ MeV/c^2) include $\phi K^{*0}(890)$ events from the tail of the $K^*(890)$ and uncorrelated $K\pi$ in the $\phi K\pi$ events.

The number of $\phi K^{*0}(890)$ events was estimated by subtracting the 43±51 fitted excess events in the $\phi K\pi$ mass plots corresponding to the $K^{*0}(890)$ side-band, seen in Fig. 5.3.8.a, from the fitted excess events in the $\phi K\pi$ mass spectrum corresponding to the $K^{*0}(890)$. Corrections for

the fact that these 43 events from the sidebands contain a small fraction of $K^{*0}(890)$ were made. The fraction (0.04) of $K^{*0}(890)$ events in the chosen side-band is calculated from the fit to the $K\pi$ spectrum. The number of correlated $\phi K^{*0}(890)$ events is then, $N[\phi K^{*0}(890)] = (166\pm46 - 43\pm51)/(1 - 0.04) = 128\pm72$.

Decays of centrally produced resonances should be charge symmetric [35]. The $\phi K^+\pi^-$ and $\phi K^-\pi^+$ mass spectra, seen in Fig. 5.3.9 yield $N[\phi K^+\pi^-]/N[\phi K^-\pi^+] = 0.8\pm.4$ consistent with unity to within the errors. Thus, the production rates of $\bar{s}d$ and $s\bar{d}$ are comparable. We also look at possible quasi-two body decay of the $K^{*0}(2060)$ in the $(\phi K)\pi$ and $(\phi\pi)K$ but no clear deviations from phase space are seen. The Dalitz plot is shown in Fig. 5.3.10.

5.4 Strange Particle Pair Production: Since the $K^{*0}(2060)$ was seen in $pN\rightarrow K^+K^-K^+K^-X$, the bachelor kaon (strange quark) with pions may form resonant states in association with the $K^*(2060)$. The $K\pi$ mass spectrum, seen in Fig. 5.4.1, for kaons and pions not used in the $K^{*0}(2060)$ mass- and side-bands shows no evidence for $K^*(890)$ or other higher K^* resonances. Also the $K\pi\pi$ and KK combinations (not shown) were looked at, but no clear effects were observed. The $\phi K\pi$ mass spectrum with another $K\pi$ in the event in the $K^{*0}(890)$ mass-band, seen in Fig. 5.4.2. shows no evidence for $pN\rightarrow K^{*0}(2060)K^{*0}(890)X$ events.

The 4-K sample was chosen because that was the trigger and hence it is less biased. For comparison, the $\phi K\pi$ mass spectrum, seen in Fig. 5.4.3, from the 378,100 $pN\rightarrow K^+K^-K^{\pm}X$ events had only a few more $K^{*0}(2060)$ events than did the 4-K sample.

5.5 $K^{*0}(2060)$ Spin-Parity: Five variables describe a three-body decay; two daughter particle center-of-mass energies and three angles that orient their decay plane. The parent spin and parity is reflected in the angular distributions of the decay plane normal [36]. The complexity of these effects increases rapidly with spin (e.g. for spin 2 the description of the angular distribution requires 15 variables. Hence, our poor statistics prevent us from carrying out such an analysis.

Similarly, the $\phi K^{*0}(890)$ two-body state and its subsequent two-body decays present distributions that reflect the spin-parity of the parent $K^{*0}(2060)$ [37]. The relevant angles are those which define the polar and azimuthal angles of the ϕ in the $\phi K\pi$ rest frame, of the K in the ϕ rest frame and of the π in the $K^{*0}(890)$ rest frame. Their definitions and distributions are seen in Fig. 5.5.1 and 5.5.2. respectively. The decay of a 4^+ state into 2 vector (1^-) mesons each decaying into 2 scalar mesons is represented by a 9 × 9 element density matrix. This has ~ 80 terms in 6 real variables to represent the decay amplitude. Our statistics, not to mention the precision of our acceptance corrections, make the unambiguous determination of the spin by any analysis impossible.

5.6 Particle Misidentification: Cherenkov algorithm inefficiencies caused real kaons to be identified as pions, for instance when one or more pion tracks above threshold threw light into the same cell occupied by the kaon. Similarly pions were identified as kaons when statistical fluctuations with a finite number of photoelectrons caused no light to

be detected. Thus, we tested for resonances in the $\phi\pi\pi$ and ϕKK which could produce reflections in the $\phi K\pi$ channel.

We Monte Carlo calculated the 2060 MeV/c^2 $\phi K\pi$ peak mass shift when the pion (kaon) was incorrectly identified as a kaon (pion), taking into account the geometry and the trigger cuts. A zero width 2060 MeV/c^2 peak in the $\phi K\pi$ mass plot would appear as a 120 MeV/c^2 wide peak centered at 2300 GeV/c^2 in a ϕKK mass plot for pions misidentified as kaons and as a 160 MeV/c^2 wide peak at 1840 MeV/c^2 in a $\phi\pi\pi$ plot for kaons misidentified as pions.

The ϕKK and $\phi\pi\pi$ mass spectra, seen in Figs. 5.6.1.a-2.a, show no structure near 2.3 and 1.8 GeV/c^2, respectively, indicating that the resonance structure at 2.079 GeV/c^2 in the $\phi K\pi$ channel is not a reflection of a resonance in the ϕKK of $\phi\pi\pi$ channels due to particle misidentification. Following the notation of Figure 4.2.2 where the momentum regions for particle identification are indicated, we tested for tracks that should appear in the π region but appear in the K/p region and vice versa. Also the $\phi K\pi$ spectra, with the pion (kaon) taken as a kaon (pion), have been plotted (Figs. 5.6.1.b-2.b) with shifted masses indicated by arrows. The absence of a clear signal at 1.8 GeV/c^2 in the $\phi\pi\pi$ channel and at 2.3 GeV/c^2 in the $\phi K\pi$ channel is also an indication that the $K^{*0}(2060)$ observed in the $\phi K\pi$ channel is not a reflection of a resonance in other channels, due to particle misidentification.

Although proton misidentification was less probable, kaons outnumbered identified protons in the proton momentum window of C_B

($20 \leq P < 38.8$ GeV/c) 60 to 1. Identified kaons in the $\phi K\pi$ combinations were defined as protons and the resulting distribution together with the $\phi p\pi$ mass spectrum, are seen in Fig. 5.6.3.

The three-body final state particle momentum distributions were not smooth because of the four-momentum regions defined by the Cherenkov thresholds and their use in the trigger. To verify that the 2060 MeV/c^2 $\phi K\pi$ peak was not produced by particle momentum distribution discontinuities, we plot the $\phi K\pi$ mass spectrum for pions in 4 momentum regions, as seen in Fig. 5.6.4.

5.7 Cross Section: The cross section (σ) is the probability of a specific final state resulting from the interaction of two initial state particles. Since the branching ratios (BRs) for the decay of the $K^{*0}(2060)$ into $\phi K\pi$ and $\phi K^{*0}(890)$ are unknown we can only give the $(d\sigma/dX_F|_{X_F=0}) \times BR$ for our two modes.

The cross section per nucleus depends on the atomic weight of the target, the A-dependence. It is expressed in terms of a power law of the form: $\sigma(A) = A^{\alpha}\sigma(A=1)$ or $\sigma_{nucleon} = \sigma(A=1)\times A^{\alpha-1}$, where A is the mass number of the target. If the nucleus is considered as a totally absorbing sphere, the projected area is proportional to $A^{\frac{2}{3}}$ thus, $\alpha = \frac{2}{3}$. However, when the interaction is supposed to occur between the constituents of the initial state hadrons, this law does not apply, and the dependence on α is expected to be $\alpha = 1$. This indeed has been measured for inclusive ϕ meson production in K^-, $\bar{p}$ and p Be interactions at 100 GeV/c to be 1.04 ± 0.04 [38]. Here we assume an $\alpha = 1$ dependence. The scintillator target is made of Pilot-B material which has an atomic

ratio H/C=1.1. The A dependence with $\alpha = \frac{2}{3}$ would introduce a factor of 2.3 reduction in cross section for carbon compared to hydrogen. This represents a 27% reduction in the cross sections calculated here.

The cross section is $\sigma = S\ N_0/A'\ A$. N_0 is the number of observed events, A the spectrometer acceptance, A' a correction for inefficiencies not included in the acceptance, and S is the nanobarn (1 b = 10^{-24} cm^2) equivalent of the experiment (i.e. the cross section for 1 event) calculated as $S = (N_t\ N_b)^{-1} = (800\ \text{events/nb})^{-1}$, where N_t is the number of target particles (6.02×10^{23}/g × (12.78(scint.) +1.92(Al) +0.53(paper)g/cm^2) or 0.918×10^{25}/cm^2 and N_b is the effective beam (the number of beam tracks corrected for dead-time) or 8.7×10^{10}.

The acceptance is a product of the geometrical acceptance (the probability that the particles in an event will traverse the magnet and chambers), the probability that at least 2 positive and 2 negative kaons will be identified by the Cherenkov counter (which include the inefficiencies and deadtimes of each cell in C_B), the trigger efficiency, and the probability that the software will reconstruct the events. Included in A' is a correction for decay of kaons before they get to Cherenkov counter C_B (0.621), the correction for unobserved decay modes (2/3), and the branching fraction of the ϕ to K^+K^- (0.49). Thus, $A' = 0.621\times0.49\times(2/3) = 0.203$.

Monte Carlo calculated acceptance samples of 20,000 $pp \rightarrow K^{*0}(2060)\overline{K}^{*0}(2060)$; $K^{*0}(2060) \rightarrow \phi K\pi$, and $\rightarrow \phi K^{*0}(890)$ events were generated with flat X_F ($|X_F| \leq 0.1$) and $\exp(-1.1P_T^2)$ distributions [21,34]. Also an $\exp(-2.5P_T^2)$ distribution for the transverse component

of momentum was tried and the results were the same as above within the errors. These events were propagated through the apparatus with a program that simulates the actual effect of the detector. For $\phi K\pi$ and $\phi K^{*0}(890)$ the 397±20 and 363±19 events which passed the acceptance cuts gave acceptance corrections of (2.0±0.1)% and (1.8±0.1)% respectively. The relative branching fraction corrected for acceptance is $\Gamma[K^{*0}(2060) \to \phi K^{*0}(890)]/[\Gamma[K^{*0}(2060) \to \phi K\pi] =$ $(128\pm72 \times 1.8\pm0.1)/(431\pm116 \times 2.0\pm0.1) = 0.3\pm0.3$.

We measured the cross section in a narrow interval in X_F:

$$\sigma_M \times B = B \int_{-.1}^{.1} \frac{d\sigma}{dX_F} dX_F = \frac{SN_0}{AA'}$$

$$= \frac{431\pm116}{800\times0.203\times(0.02\pm0.001)} = 133\pm36 \text{ nb.}$$

Assuming a X_F distribution

$$\frac{d\sigma}{dX_F} = \left.\frac{d\sigma}{dX_F}\right|_{X_F=0} (1 - |X_F|)^n ,$$

we get

$$B \int_{-.1}^{.1} \frac{d\sigma}{dX_F} dX_F = B \left.\frac{d\sigma}{dX_F}\right|_{X_F=0} \int_{-.1}^{.1} (1 - |X_F|)^n \, dX_F$$

$$= B \left.\frac{d\sigma}{dX_F}\right|_{X_F=0} \frac{2}{n+1} (1 - 0.9^{n+1})$$

and solving for $B \, d\sigma/dX_F|_{X_F=0}$ with $n = 2.8$:

$$B \left.\frac{d\sigma}{dX_F}\right|_{X_F=0} = 765 \pm 209 \text{ nb.}$$

Assuming a X_F distribution we can extrapolate to get the total cross section $\sigma_T \times B = 2B(d\sigma/dX_F|_{X_F=0})/(n+1)$. Using the value of $n = 2.8$ and $n = 1.8$ measured for the $K^{*0}(890)$ by experiment E580 [19] and the ACCMOR group [32], the $\sigma_T \times B(\rightarrow \phi K\pi)$ are 403±110 nb and 520±285 nb respectively.

We can estimate the total cross section using the phenomenological model of Bourquin and Gaillard [33] and thus derive the branching ratios to $\phi K\pi$ and $\phi K^{*0}(890)$. In this model, the inclusive total cross section for production of a mass m is given by:

$$\sigma(\mu b) = 0.4 \times 10^{10} \, y_{max}^2 \exp(-5.13/y_{max}^{0.38}) \frac{M}{(M+2)^{12.3}}$$

M is the mass of the simplest "composite" particle consistent with the production of m and local conservation of quantum numbers, y_{max} is the maximum rapidity in the center of mass (CM) $y_{max} = \ln[(E_{cm}^{max} + p_{cm}^{max})/m]$, p_{cm}^{max} and E_{cm}^{max} are respectively the maximum momentum and energy of the composite particle with mass M in the center of mass system. M takes the value of the $K^*(2060)$ mass plus an additional 490 MeV/c^2 to form the

composite mass required in the model. The results of this calculation gives $\sigma[pp \rightarrow K^{*0}(2060)X] = 11$ μb, thus the total cross section for production of $K^{*0}(2060) + \bar{K}^{*0}(2060)$ would be 22 μb. Assuming the validity of the Bourquin-Gaillard model and $n = 2.8$, the $K^{*0}(2060)$ branching fractions for the $\phi K\pi$ and the $\phi K^{*0}(890)$ are 1.8% and 0.6% respectively.

We conclude that a high mass K^*, the $K^{*0}(2060)$ has been observed with a mass of 2079±7 MeV/c^2 and width 61±58 MeV/c^2, decaying into $\phi K\pi$ and $\phi K^{*0}(890)$, the $(d\sigma/dX_F|_{X_F=0}) \times BR(\rightarrow\phi K\pi)$ corrected for acceptance and detection efficiency is 765±209 nb, and the relative branching ratio is $\Gamma[K^{*0}(2060) \rightarrow \phi K^{*0}(890)]/[\Gamma[K^{*0}(2060) \rightarrow \phi K\pi] = 0.3\pm0.3$.

REFERENCES

1. H. Yukawa, Proc. Phys. Math. Soc. Japan. 17, 48 (1935).

2. R. Feynman, Phys. Rev. 74, 1430 (1948); and J. Schwinger, Phys. Rev. 73, 416 (1948).

3. S. Meshkov, in Recent Developments in High Energy Physics, edited by B. Kursunoglu (Plenum, New York, 1981).

4. S.L. Glashow, Nucl. Phys. 22, 579 (1961); S. Weinberg, Phys. Rev. Lett. 19, 1264 (1967); and A. Salam, Rev. Mod. Phys. 53, 539 (1980).

5. J. Goldstone, Nuovo Cimento 19, 15 (1961).

6. G. 't Hooft, Nucl. Phys. B35, 167 (1971).

7. M. Gell-Man, Phys. Lett. 8, 214 (1964); and G. Zweig, CERN preprint (unpublished) (1964).

8. J.J. Aubert et al., Phys. Rev. Lett. 33, 1404 (1974); and J.J. Augustin et al., Phys. Rev. Lett. 33, 1406 (1974).

9. S.W. Herb et al., Phys. Rev. Lett. 39, 252 (1977).

10. L. Jones, Rev. Mod. Phys. 49, 722 (1977).

11. C.G. Wohl, et al. [Particle Data Group], Rev. Mod. Phys. , 56, S1 (1984).

12. G.F. Chew and S.C. Frautschi, Phys. Rev. Lett. 8, 41 (1962).

13. D.D. Carmony et al., Phys. Rev. Lett. 27, 1160 (1971); and Phys. Rev. D16, 1251 (1977).

14. C. Bromberg et al., Phys. Rev. D22, 1513 (1980).

15. D. Aston et al., Phys. Lett. B99, 502 (1981); and Phys. Lett. B106, 235 (1981).

16. M. Baubillier et al., Phys. Lett. B118, 447 (1982).

17. W.E. Cleland et al., Phys. Lett. B97, 465 (1980).

18. J. Poirier, et al., in Multiparticle Dynamics 1981, edited by R. Kinney and W.D. Shepard (World, Singapore, 1982) pp.153-160; T.Y. Chen et al., Phys. Rev. D28, 2304 (1983); C.C. Chang et al., Phys. Rev. D29, 1888 (1984); H.C. Fenker et al., Phys.

Rev. D30, 872 (1984); E.G.H. Williams et al., Phys. Rev. D30, 877 (1984); and J. Ficenec, et al., in Multiparticle Dynamics 1983, edited by P. Yager and J.F. Gunion (World, Singapore, 1984) pp.491-499.

19. A. Napier et al., Phys. Lett. B (to be published).

20. S. Okubo, Phys. Lett. 5, 163 (1963).

21. C. Georgiopoulos, et al., Phys. Lett. B (to be published).

22. F. Davenport, Ph.D. thesis, Florida State University, 1984.

23. F. Sauli, CERN 77-09 (1977).

24. A.S. Vovenko et al., Sov. Phys. USPEKHI 6, 794 (1964).

25. H.C. Fenker, D.R. Green, S. Hansen and T.F. Davenport, FERMILAB-82/62-EXP (unpublished).

26. TID-25875-7 (USAEC, Washington, 1972).

27. J. Jelley, Cherenkov Radiation and Its Applications,, (Pergamon, New York, 1958); and V.P. Zrelov, Cherenkov Radiation in High Energy Physics, transl. by Y. Oren, edited by Benny Baruch (U.S. Clearinghouse, Springfield, 1970).

28. J.R. Johnson et al., Phys. Rev. D17, 1292 (1978).

29. C. Georgiopoulos, Ph.D. Thesis, Tufts University, 1985.

30. M. Atkinson, et al., CERN EP/84-106 (1984); M. Barth et al., Phys. Lett. B117, 267 (1982); C. Daum et al., Phys. Lett. B96, 313 (1982) and Nucl. Phys. B186, 205 (1981); T. Armstrong, et al., Nucl. Phys. B224, 193 (1983); R. Barate, et al., Phys. Lett. B121, 449 (1983); and R. Jongerius, Ph.D. Thesis, NIKHEF, 1982.

31. R.P. Feynman, Phys. Rev. Lett. 23, 1415 (1969).

32. R. Bailey, Z. Phys. 24, 111 (1984).

33. M. Bourquin and J.M. Gaillard, Nucl. Phys. B114, 334 (1976).

34. E. Byckling and K. Kajantie, Particle Kinematics, (Wiley, N.Y. 1973).

35. W. Kittel, in Partons in Soft-Hadronic Processes, edited by R.T. Van de Walle (World Scientific, Singapore, 1981); V.V.

Anisovich and V.M. Shekhter, Nucl. Phys. B55, 455 (1973); V.V. Anisovich and M.N. Kobrinsky, Phys. Lett. B5, 357 (1981); and V.V. Anisovich et al., Nucl. Phys. B55, 474 (1973).

36. S.M. Berman and M. Jacob, Phys. Rev. 139, 1023 (1965).

37. S.U. Chung, Phys. Rev. 169, 1342 (1968); and J.D. Richman, CALT-68-1148 (1984).

38. C. Daum et al., Z. Phys. 18, 1 (1983).

Table 1.1. Summary of observed $K^*(2060)$ states.

J^P	Mass	Width	Mode	Ratio		$\sigma(\mu b)\times BR$	ref.
4^+	2094 ± 65	540 ± 300	$K^{*0}\to K^+\pi^-$	$K^*(1420)\pi/K\pi$	0.45 ± 0.18		13
				$K^*(890)\rho/K\pi$	0.18 ± 0.10		
	2146 ± 30	52 ± 50	$K^{*0}\to K^0(\pi\pi)^0$	$K^*(890)\pi/K\pi$	0.17 ± 0.07		
				$K\rho/K\pi$	0.16 ± 0.06		
				$Kf/K\pi$	0.05 ± 0.02		
-	2003 ± 14	87 ± 43	$K^{*0}\to K^0A_2(1320)$			0.26 ± 0.03	14
4^+	$2070^{+100}_{-\ 40}$	240^{+500}_{-100}	$K^{*0}\to K^-\pi^+$	$K\pi/all$	0.07 ± 0.01		15†
-	2088 ± 20	$170^{+100}_{-\ 50}$	$K^{*-}\to\bar{K}^0\pi^-$			3.6 ± 1.2	16
			$K^{*-}\to K^{*-}(890)(\pi\pi)^0$			3.2 ± 1.6	
			$K^{*-}\to K^{*-}(890)(\pi\pi\pi)^0$			2.7 ± 1.5	
			$K^{*-}\to\bar{K}^0\rho^-$			2.1 ± 0.9	
			$K^{*-}\to\bar{K}^0\omega\pi^-$			1.8 ± 0.9	
4	2023 ± 10	324 ± 45	$K^{*-}\to K^0\pi^\pm$				17
-	2079 ± 10	71 ± 55	$K^{*0}\to\phi(K\pi)^0$	$\phi K^{*0}(890)/\phi K\pi$	0.4 ± 0.2	0.35 ± 0.08	this
			$\to\phi K^{*0}(890)$			0.14 ± 0.08	expt

† This is a Partial Wave Analysis all others are production experiments.

Table 1.2. Possible $\phi K\pi$ final states of $K^*(2060)$.

Reaction		Threshold MeV/c^2	Observed here	Acceptance %	Events/ Upper Limits
$K^{*0}(2060)$	$\rightarrow \phi(K\pi)^0$	1653	yes	1.9	431±116
	$\rightarrow \phi K^{*0}(890)$	1912	yes	1.8	128±72
	$\rightarrow \phi(K\pi\pi\pi)^0$	1932	no	1.2	< 0.003
$K^{\pm *}(2060)$	$\rightarrow \phi K^{\pm}$	1513	no	0.8	< 145
	$\rightarrow \phi K^{\pm}(\pi\pi)^0$	1792	no	1.3	< 2
	$\rightarrow \phi K^{\pm}(\pi\pi\pi\pi)^0$	2071	no	0.5	< 0.00002
	$\rightarrow \phi K^{*0}(890)\pi^{\pm}$	2072	no	0.1	< 0.3

Table 2.2.1. Drift chambers physical characteristics.

Aperture	3.352 × 1.676 m^2
Gas	argon(.574) ethane(.426)
Space resolution	300 μm
Sense wires	0.0254 mm Au plated W @75g tension
Field shaping wires	0.0635 mm Cu-Be @220g tension
Sense wire spacing	1.905 cm

Table 2.3.1. Cherenkov C_B physical characteristics.

Dimensions	226 × 122 × 330 cm^3
Mirror area	322 × 142 cm^2
Gas	N_2
Refractive index	1.0003
Radiator length	177 cm
Cone radius (β=1)	4 cm
Mirrors	30
Mirror to target	5.6 m
Pion threshold	5.7 GeV/c
Kaon threshold	20.0 GeV/c
Proton threshold	38.8 GeV/c

Table 3.1.1. Trigger rates.

Name	Trigger	σ(μb)
IB(=σ_I)	-	30,000
E	-	8,760
EG	-	1,077
2K	EG • $K^+(1,4)$ • $K^-(1,4)$	377
ϕ	2K • (ML + MR)	121
4K	EG • $K^+(=2,4)$ • $K^-(=2,4)$	94
2Kϕ	4K • (ML + MR)	51
$\phi\phi$	4K • (ML • MR)	12

Table 4.2.1. Cherenkov C_B operational characteristics.

Mirror number	Default pedestal	Most prob. channel*	One p.e. channel*	Dead %	Overflow %	ε %
1	25	0	0	0.0	0.0	0.0
2	19	64	27	2.4	0.0	4.5
3	25	52	17	0.0	0.0	5.8
4	19	32	12	5.7	0.0	5.0
5	21	30	10	1.1	0.0	5.7
6	20	64	23	4.6	0.0	5.3
7	21	54	24	10.1	0.0	4.2
8	21	48	14	1.4	0.0	6.5
9	21	66	12	10.0	0.0	10.4
10	21	48	18	0.8	0.0	5.0
11	22	60	12	73.9	1.4	9.4
12	22	60	13	49.1	1.5	8.7
13	21	70	14	48.9	4.2	9.4
14	20	72	10	55.2	4.5	13.6
15	32	60	17	52.2	1.0	6.7
16	21	100	15	59.4	4.3	12.6
17	10	80	24	42.7	6.5	6.3
18	10	76	14	54.7	6.8	10.2
19	8	60	10	62.4	7.5	11.3
20	0	80	17	79.2	0.5	8.9
21	9	32	10	37.3	0.0	6.0
22	11	24	10	22.2	0.0	4.5
23	9	32	19	40.3	0.0	3.2
24	12	39	10	32.8	0.0	7.4
25	21	40	17	0.0	0.0	4.4
26	21	144	30	0.0	0.0	9.1
27	21	120	20	0.0	0.0	11.3
28	22	60	14	0.0	0.0	8.1
29	21	84	20	0.0	0.0	7.9
30	20	17	10	0.0	0.0	3.2

*Pedestal subtracted.

Table 4.3.1. Cherenkov decision multiplicities.

Region	Tracks	
	positive	negative
e and π/K/p low	99,943	93,967
π	38,090	31,740
π/K	26,950	18,400
π/K/p high	66,081	28,950
K/p	324,570	318,190
p	6,370	4,210
Inefficiency ($P \geq 38.8$ GeV/c and no light)	5,370	3,620

Table 5.1.1. Data fit parameters.

χ^2/DF	M_0 (GeV/c^2)	α	β (GeV/c^2)$^{-1}$	M (MeV/c^2)	Γ(FWHM) (MeV/c^2)	Events	Fig.
61/79	0.9874±0.0001	0.316±0.002	8.9±0.4	1019.6±0.3	9.6±0.6	3787±199	5.1.1
36/30	1.67±0.001	0.61±0.03	2.84±0.08	2048±10	60±59	502±188	5.2.1†
16/23	1.79±0.006	1.21±0.02	2.49±0.05	2079±7	61±58	431±116	5.2.2†
36/26	1.78±0.01	1.4±0.2	3.0±0.3	-	-	-	5.2.3
21/18	0.720±0.006	0.69±0.08	2.3±0.2	892*	52±26	305±91	5.3.1
14/21	1.243±0.01	4.0 ±0.1	8.3±0.2	2079*	61*	166±46	5.3.8.a†
20/23	1.5±0.1	4.1 ±0.4	11±1	2079*	61*	43±51	5.3.8.b†
27/22	1.78±0.02	1.33 ±0.05	2.92±0.08	2079*	75*	147±62	5.3.9.a
33/23	1.76±0.01	1.61 ±0.05	2.93±0.08	2079*	75*	190±62	5.3.9.b

* fixed in the fit.
† a Breit-Wigner convoluted with a Gaussian resolution function was used in the fit.

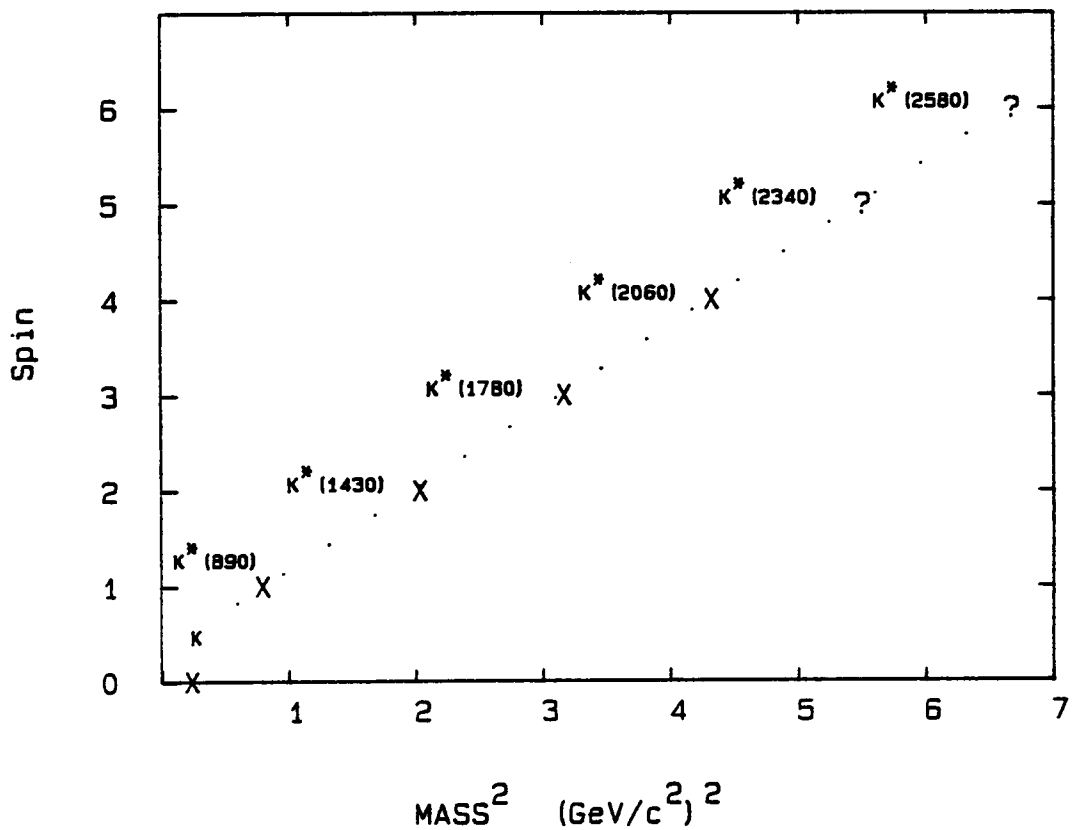

Fig. 1.1: Kaon Regge trajectory.

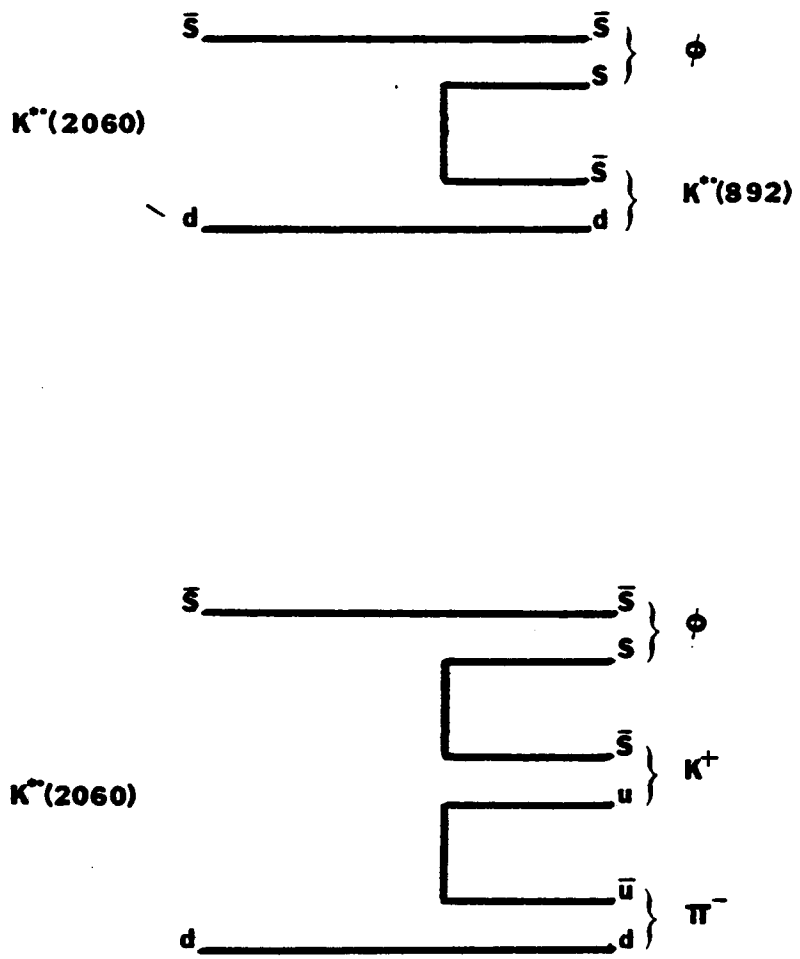

Fig. 1.2: Some quark diagrams for observed states.

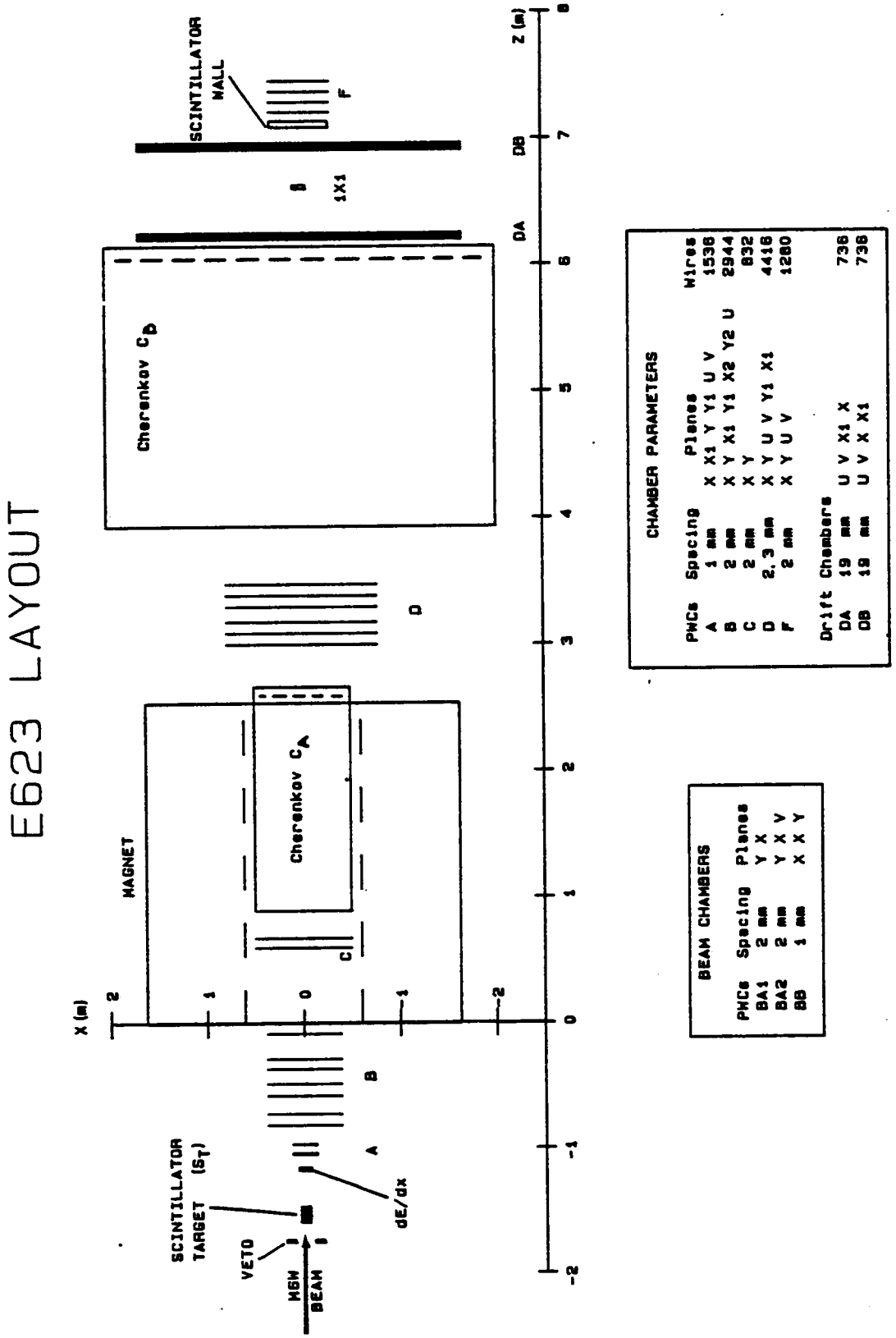

Fig. 2.1.1: Plan view of experimental apparatus.

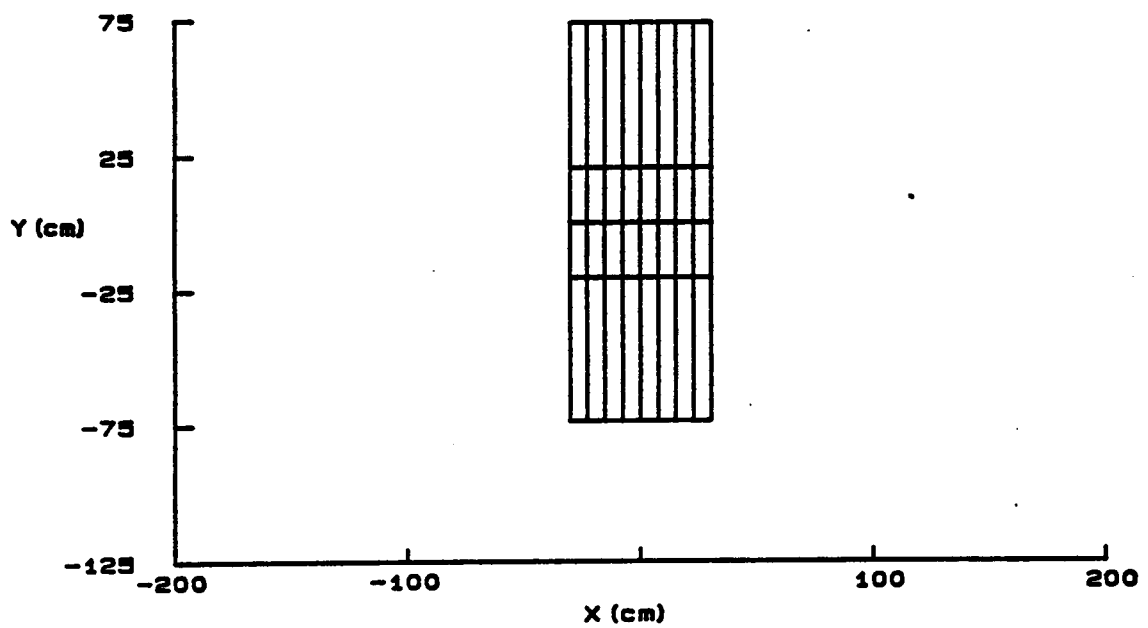

Fig. 2.1.2: Scintillator wall segmentation.

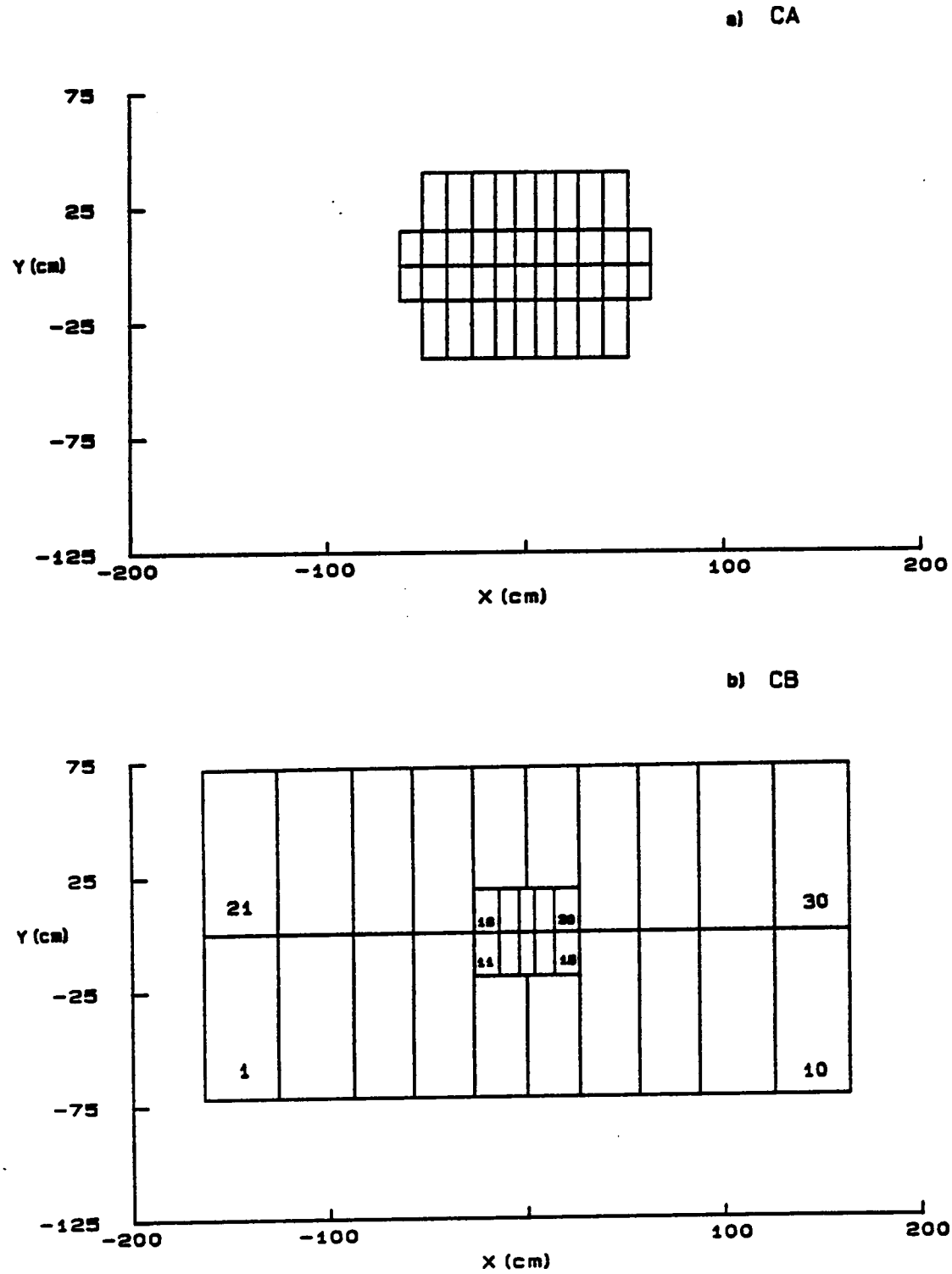

Fig. 2.3.1: Cherenkov segmentation (a) C_A and (b) C_B.

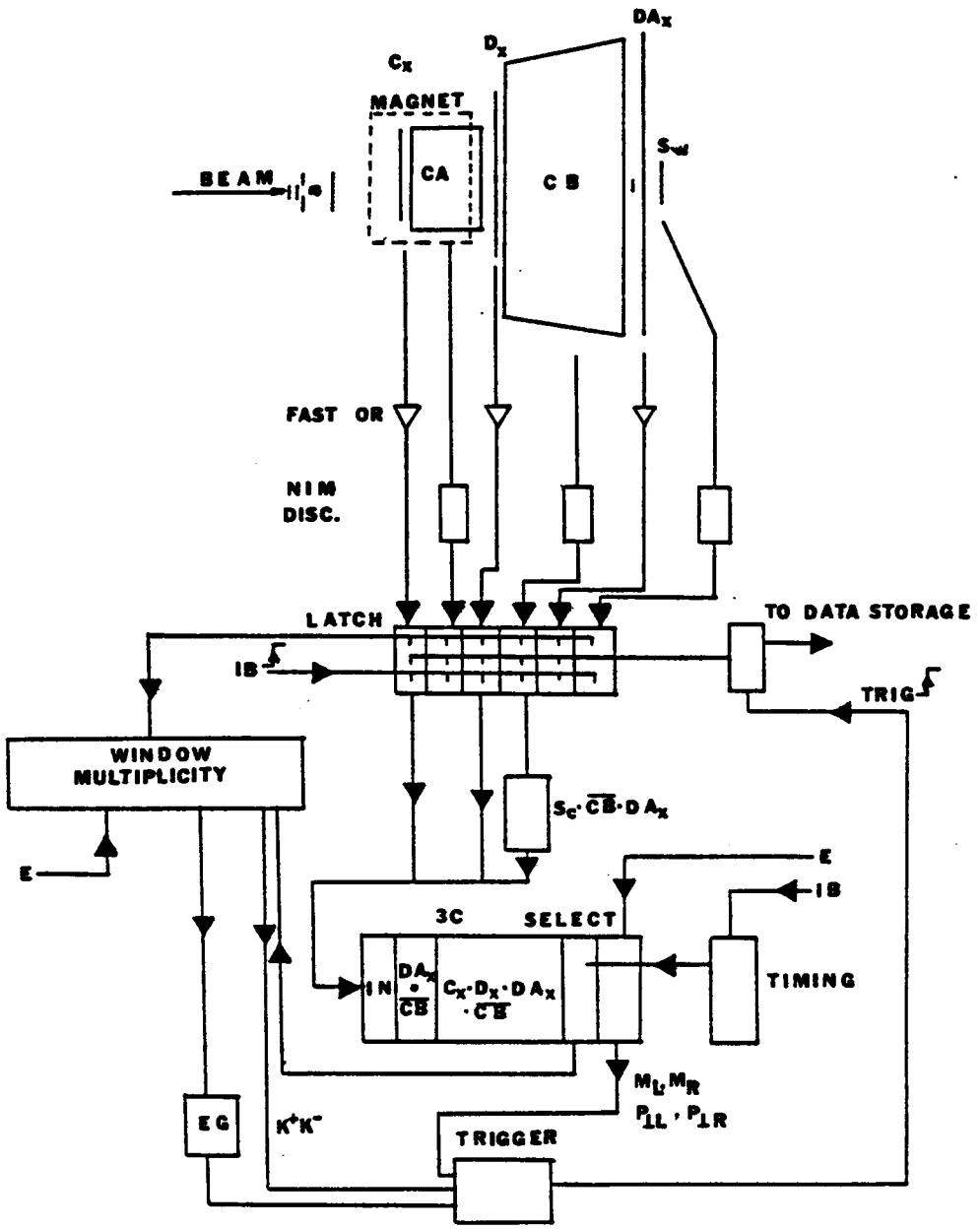

Fig. 3.1.1: Schematic of the trigger logic [25].

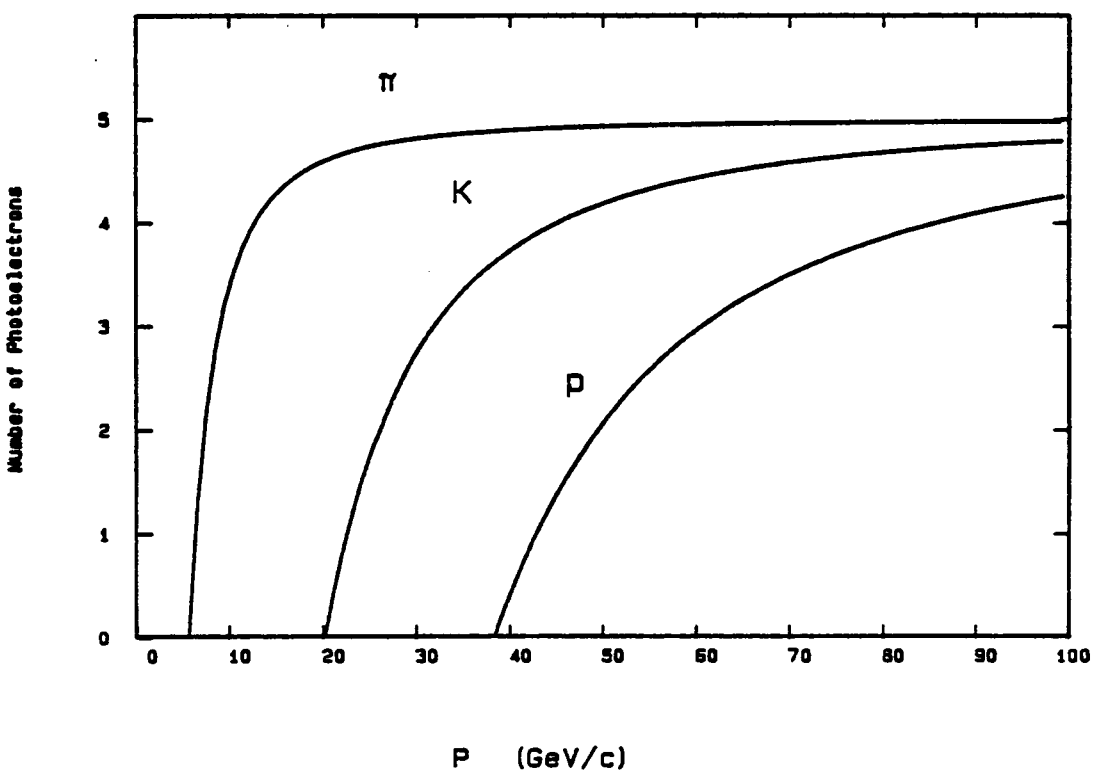

Fig. 4.2.1: The photoelectron yield with particle momentum.

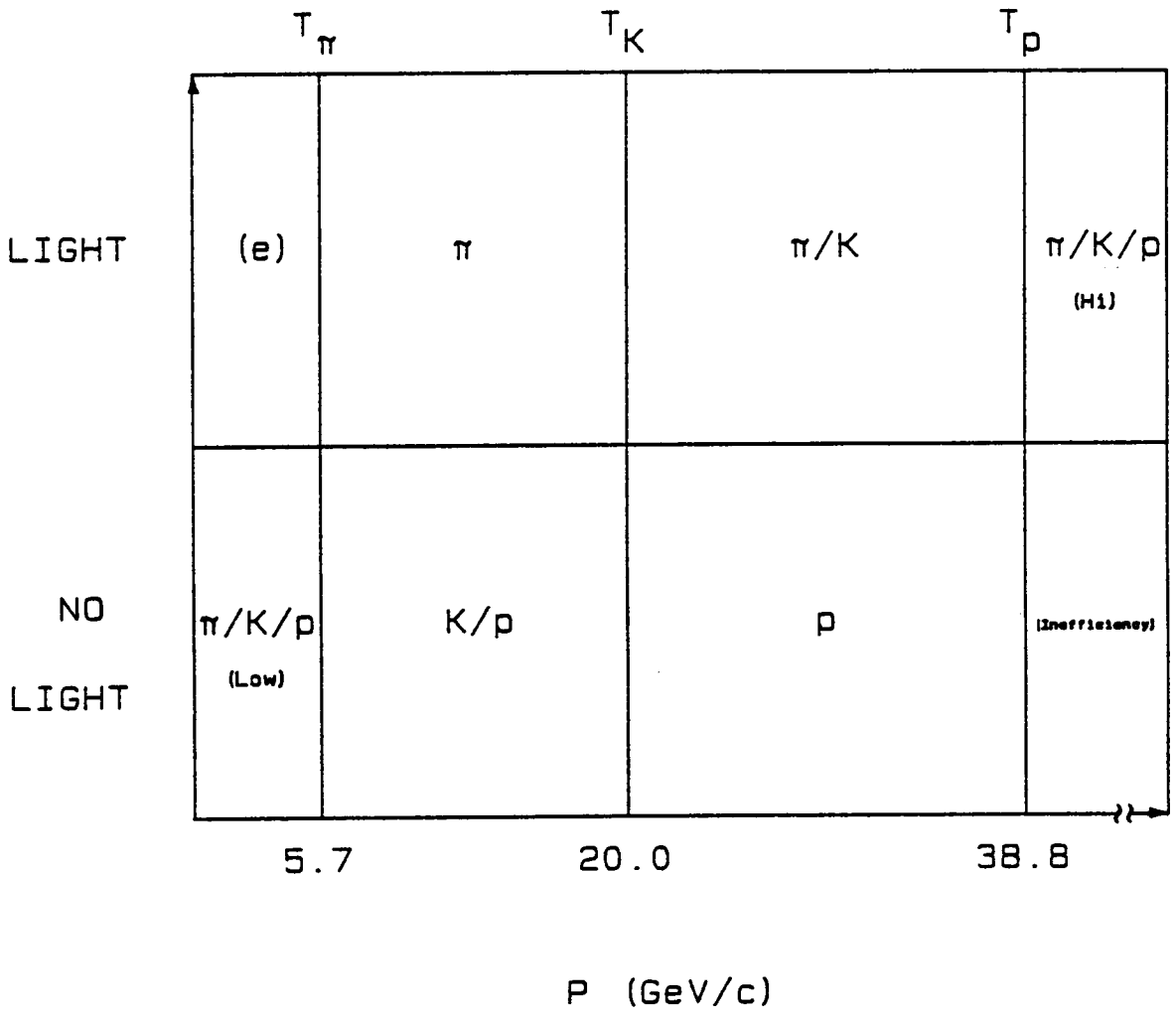

Fig. 4.2.2: Particle identification momenta regions for nitrogen.

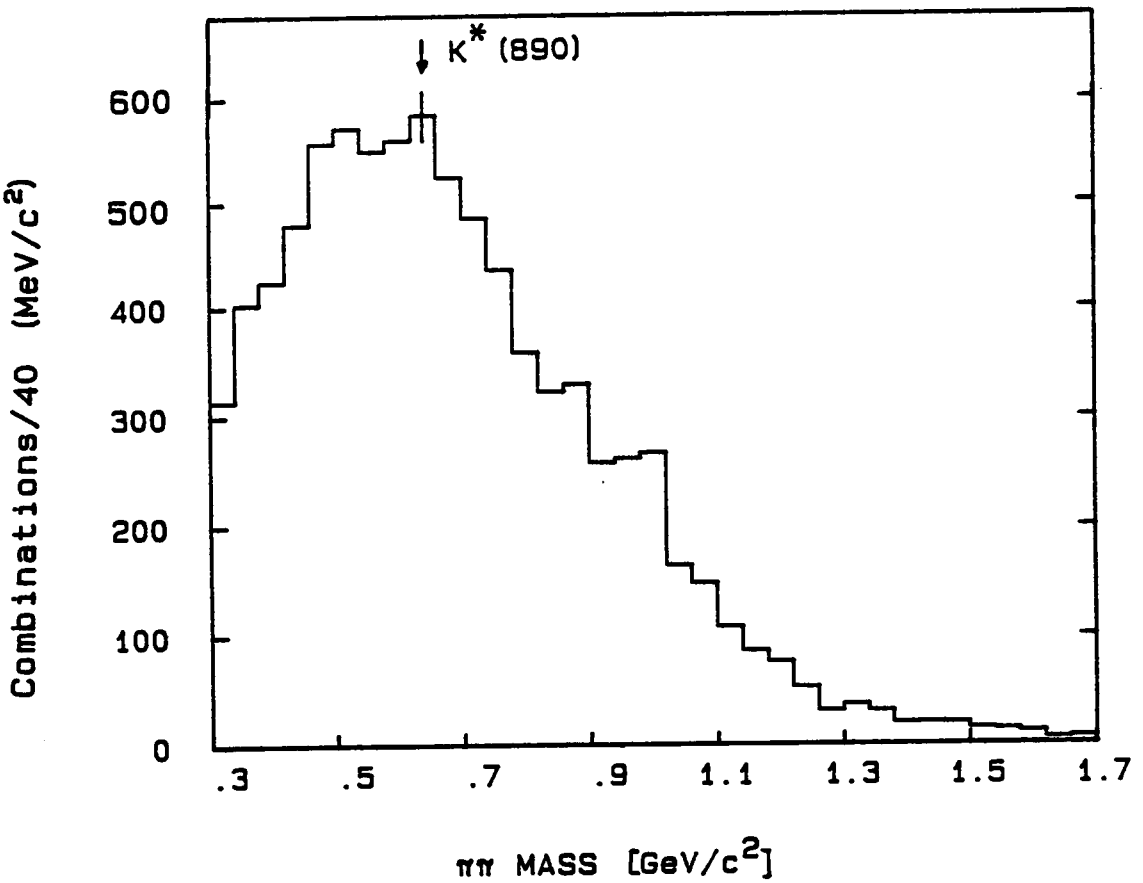

Fig. 4.3.1: The ππ mass spectrum.

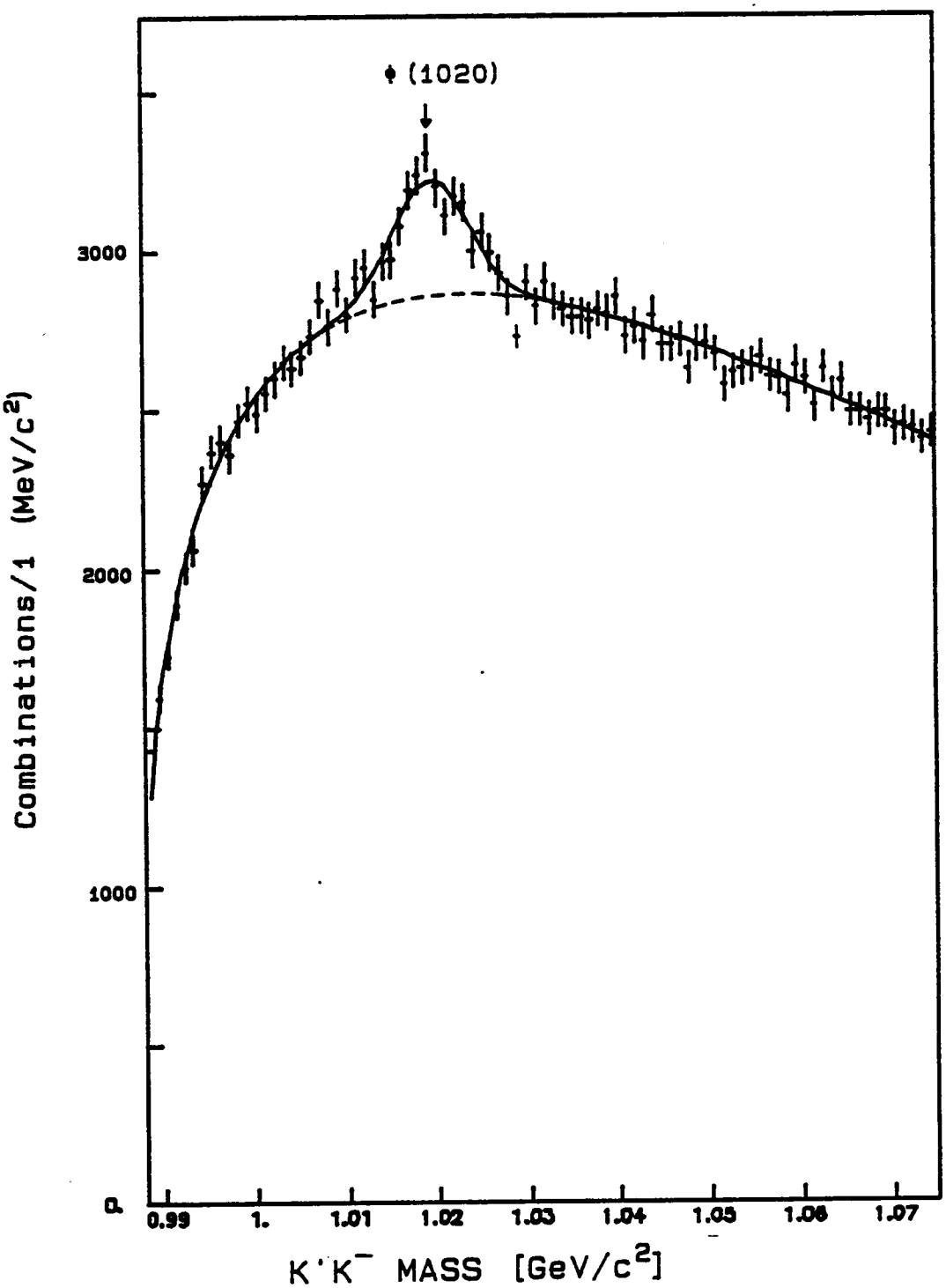

Fig. 5.1.1: The K^+K^- mass spectrum.

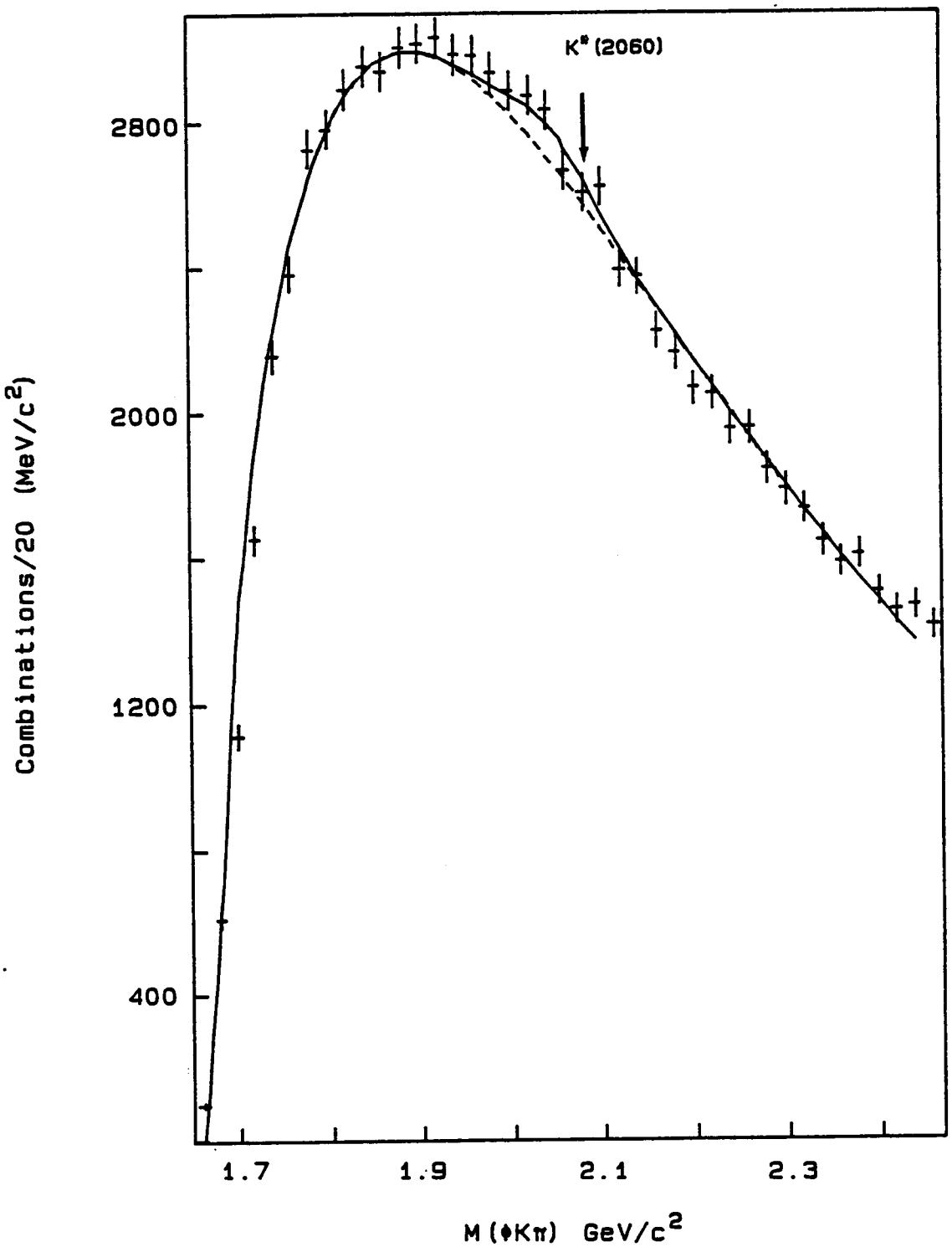

Fig. 5.2.1: The $\phi K\pi$ mass spectrum ($P < 5.8$ GeV/c tracks included).

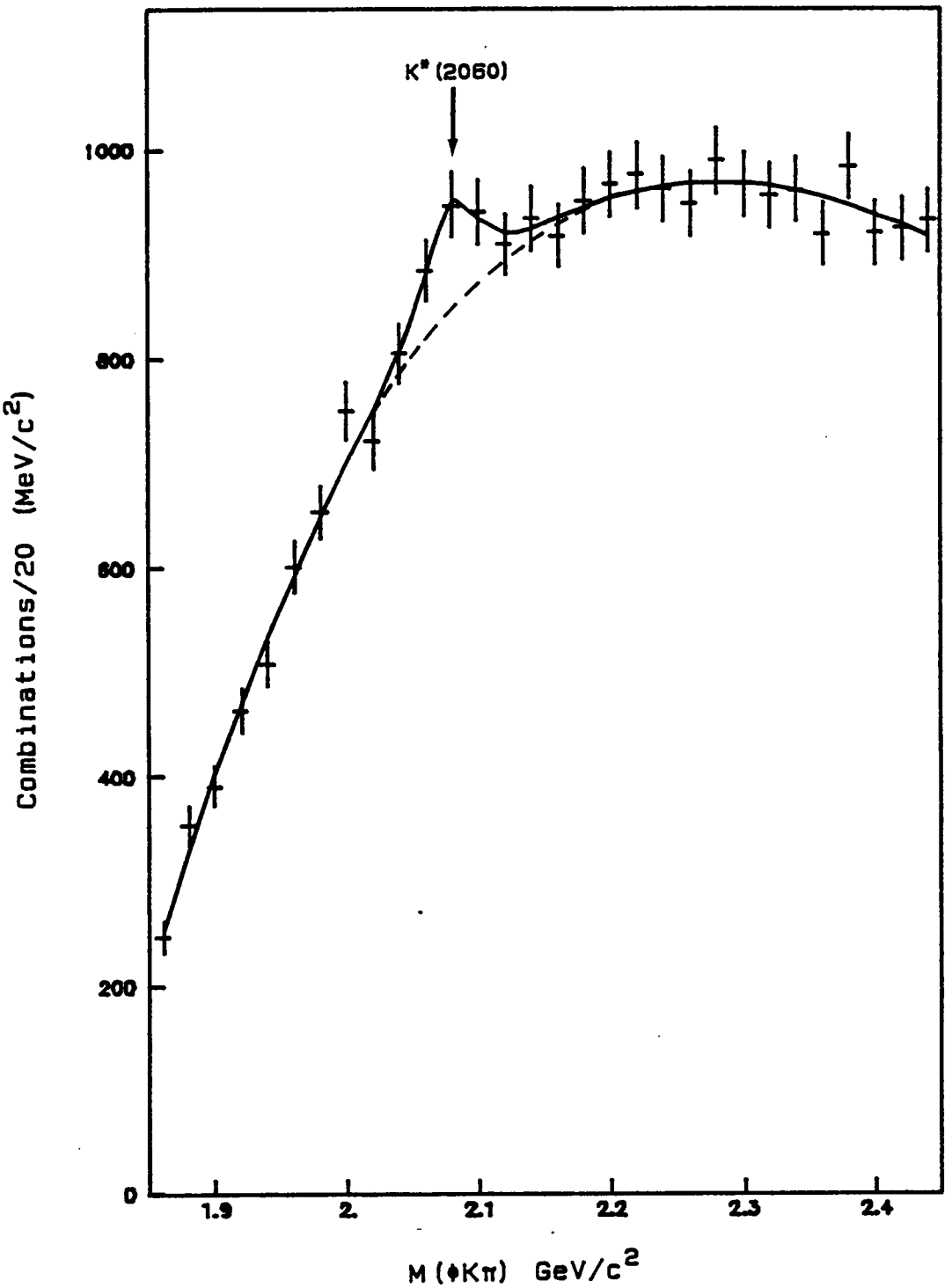

Fig. 5.2.2: The $\phi K\pi$ mass spectrum.

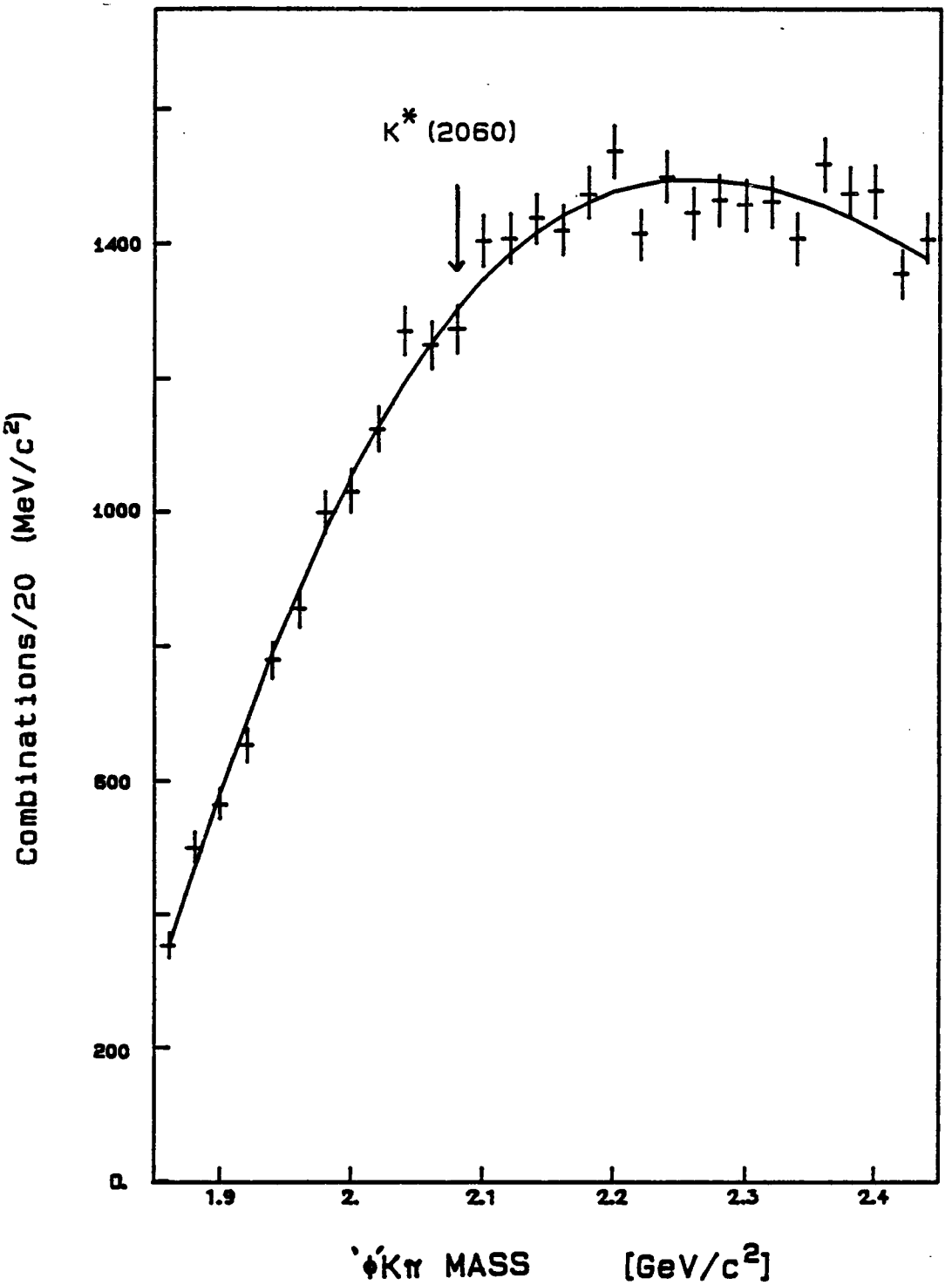

Fig. 5.2.3: The 'φ'Kπ φ side-band mass spectrum.

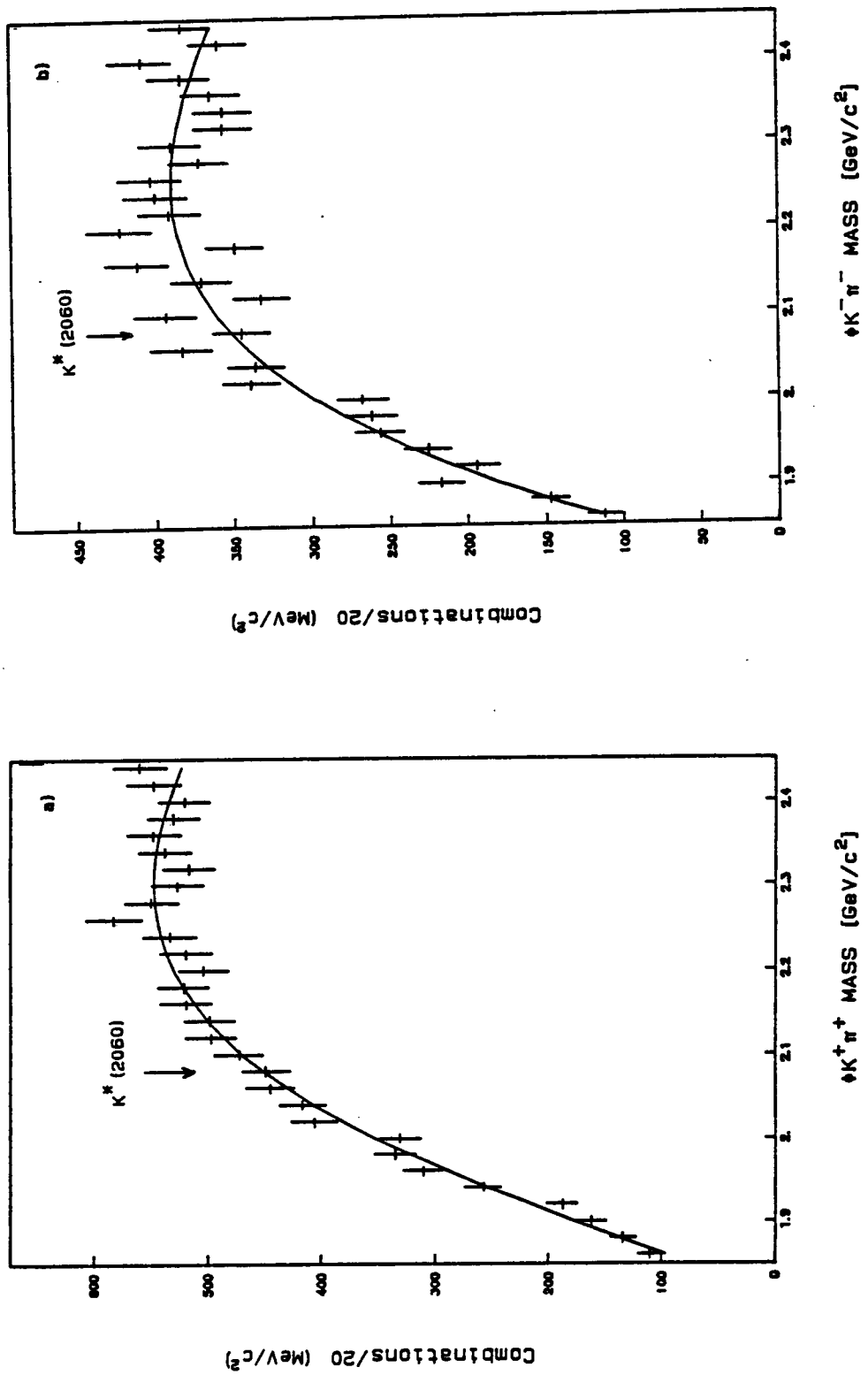

Fig. 5.2.4: Mass spectra for (a) $\phi K^+\pi^+$ and (b) $\phi K^-\pi^-$.

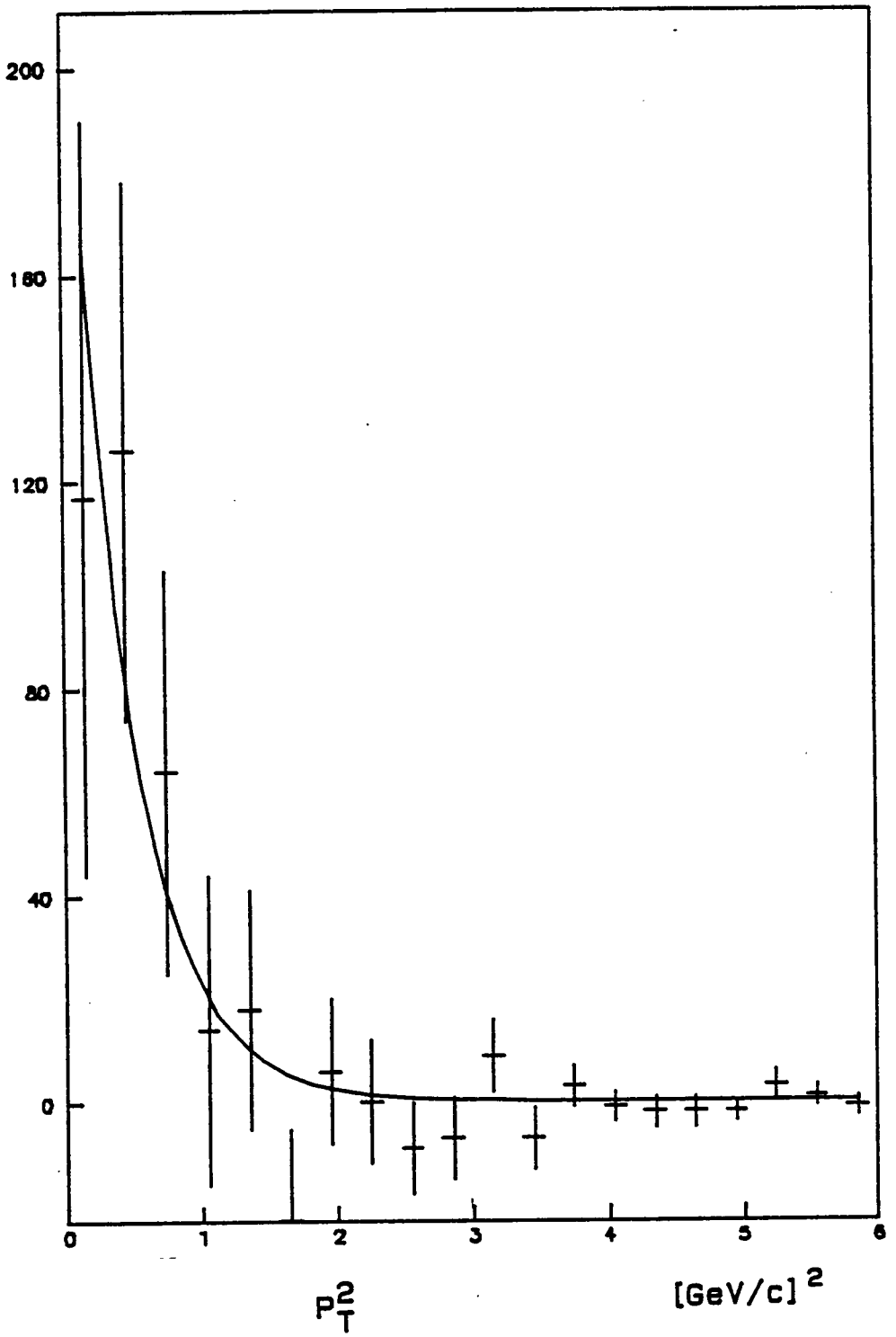

Fig. 5.2.5: The $K^{0*}(2060)$ P_T^2 distribution.

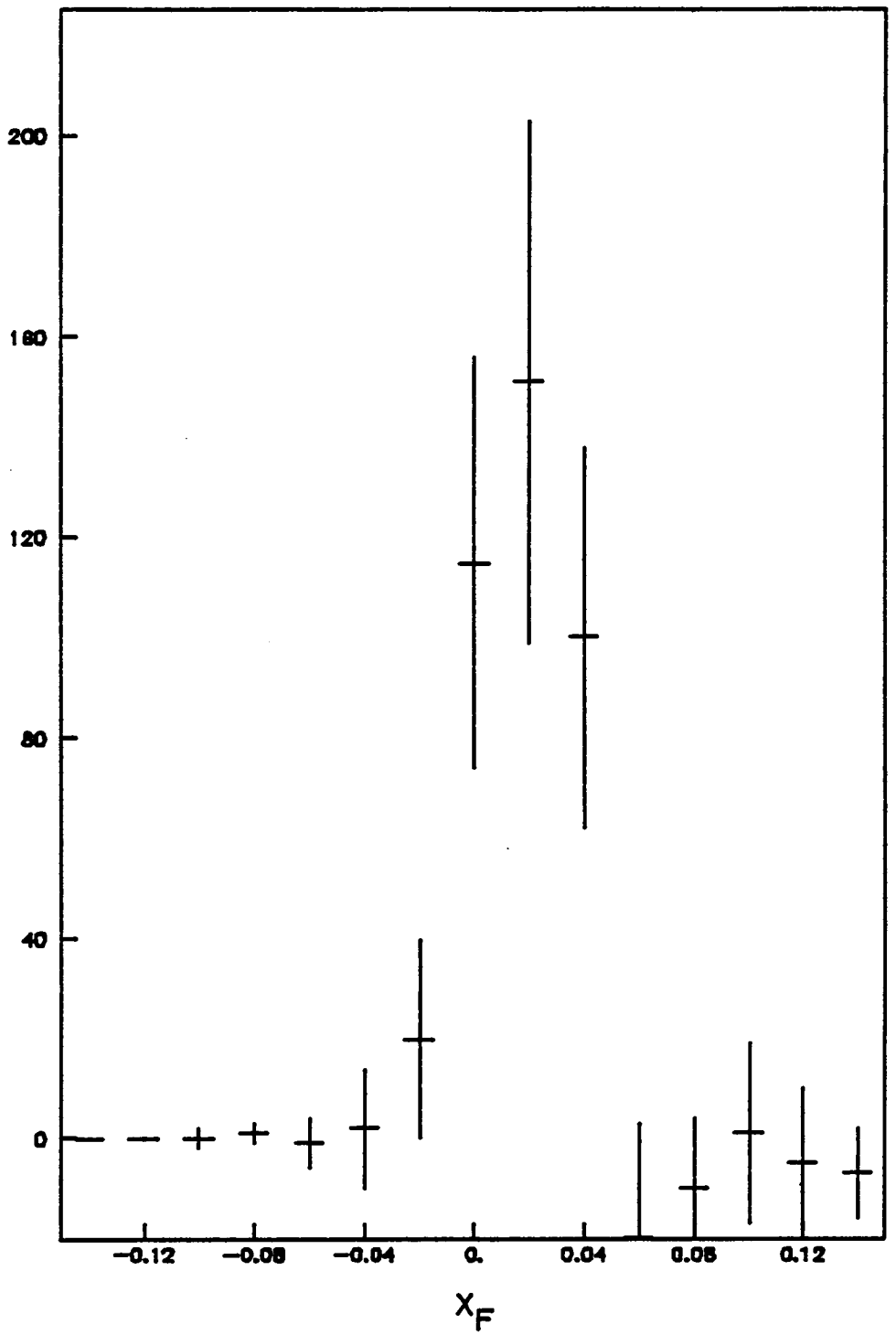

Fig. 5.2.6: The $K^{o*}(2060)$ X_F distribution.

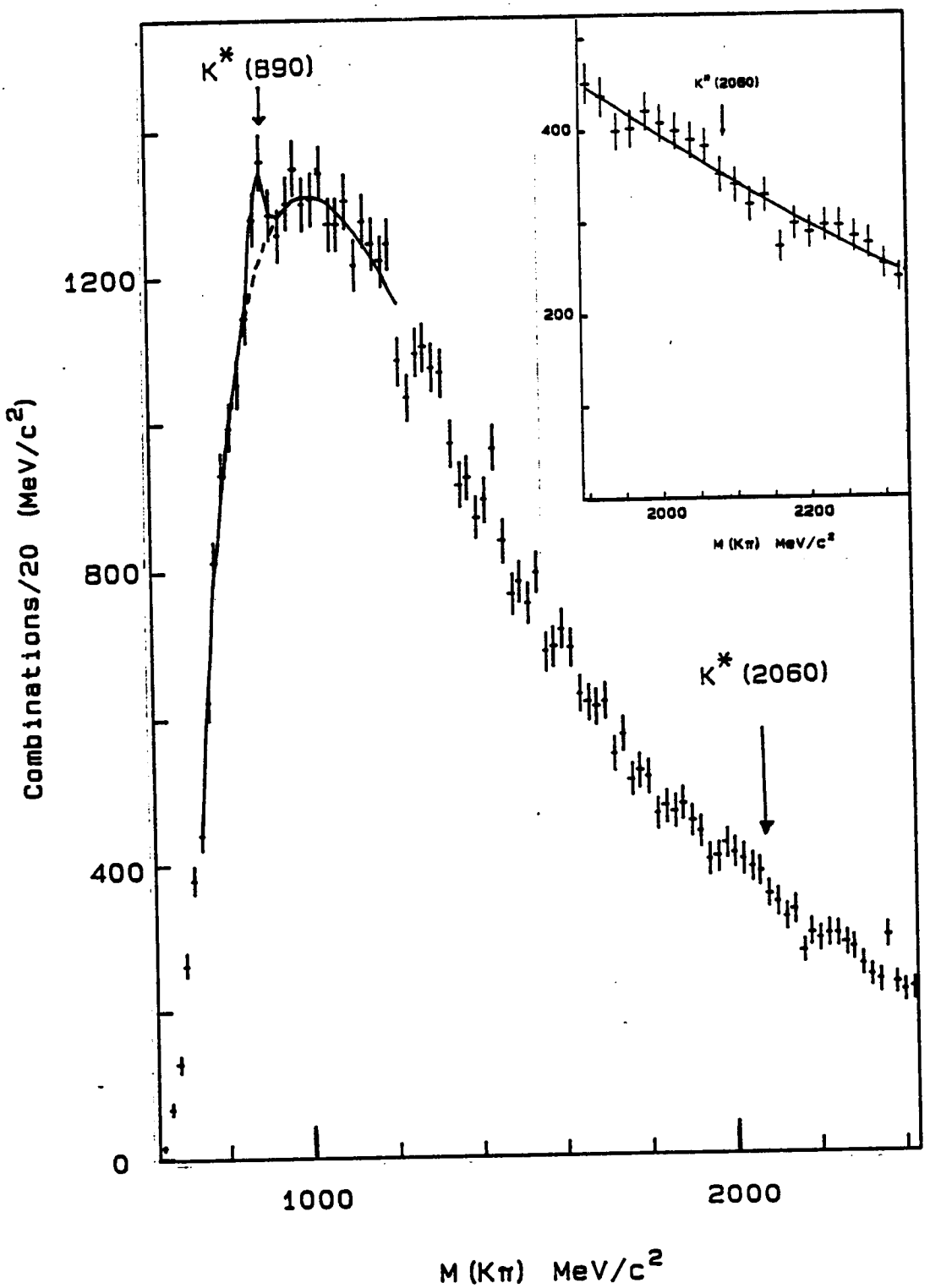

Fig. 5.3.1: The $(K\pi)^0$ mass spectrum.

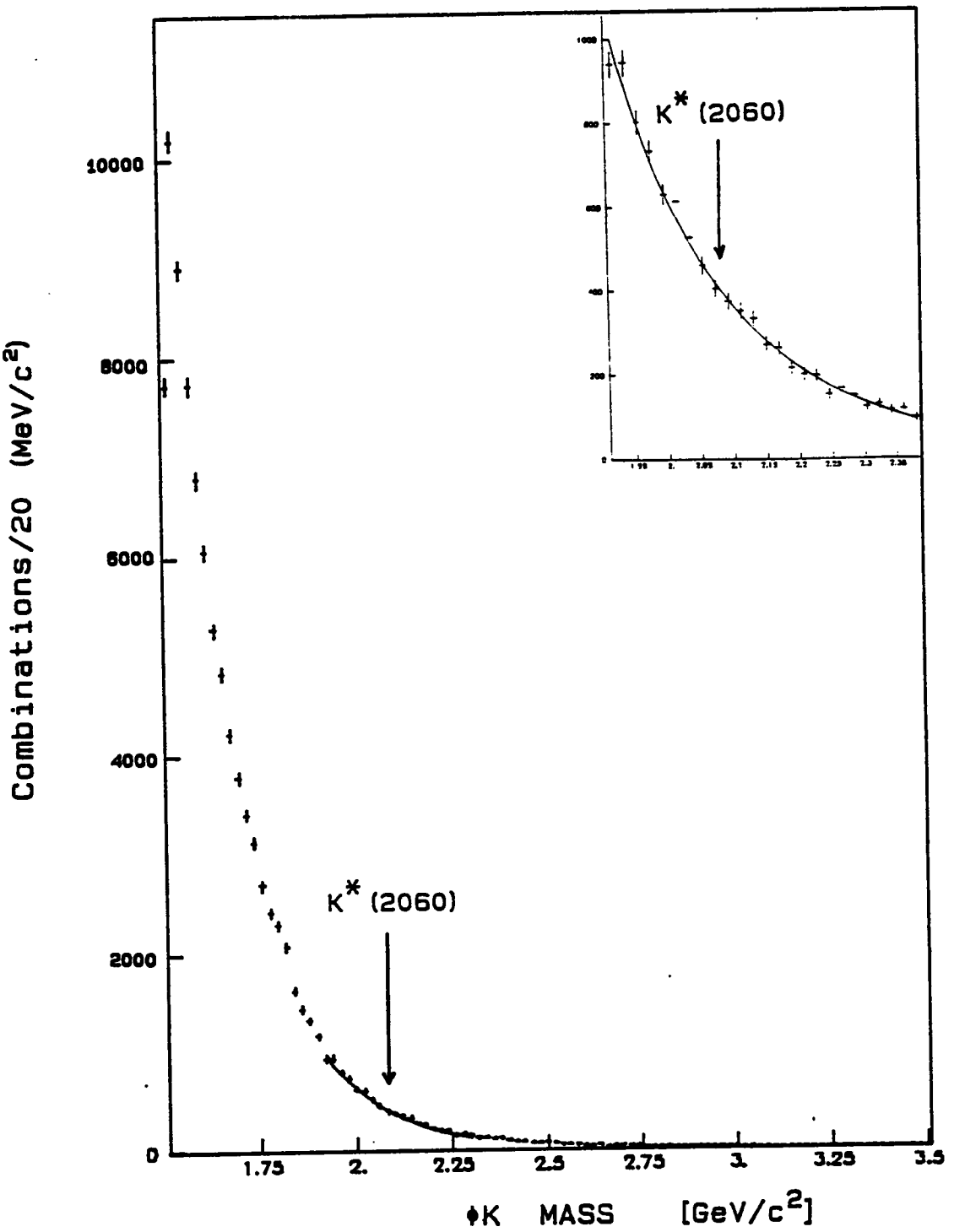

Fig. 5.3.2: The $\phi K^{\pm}$ mass spectrum.

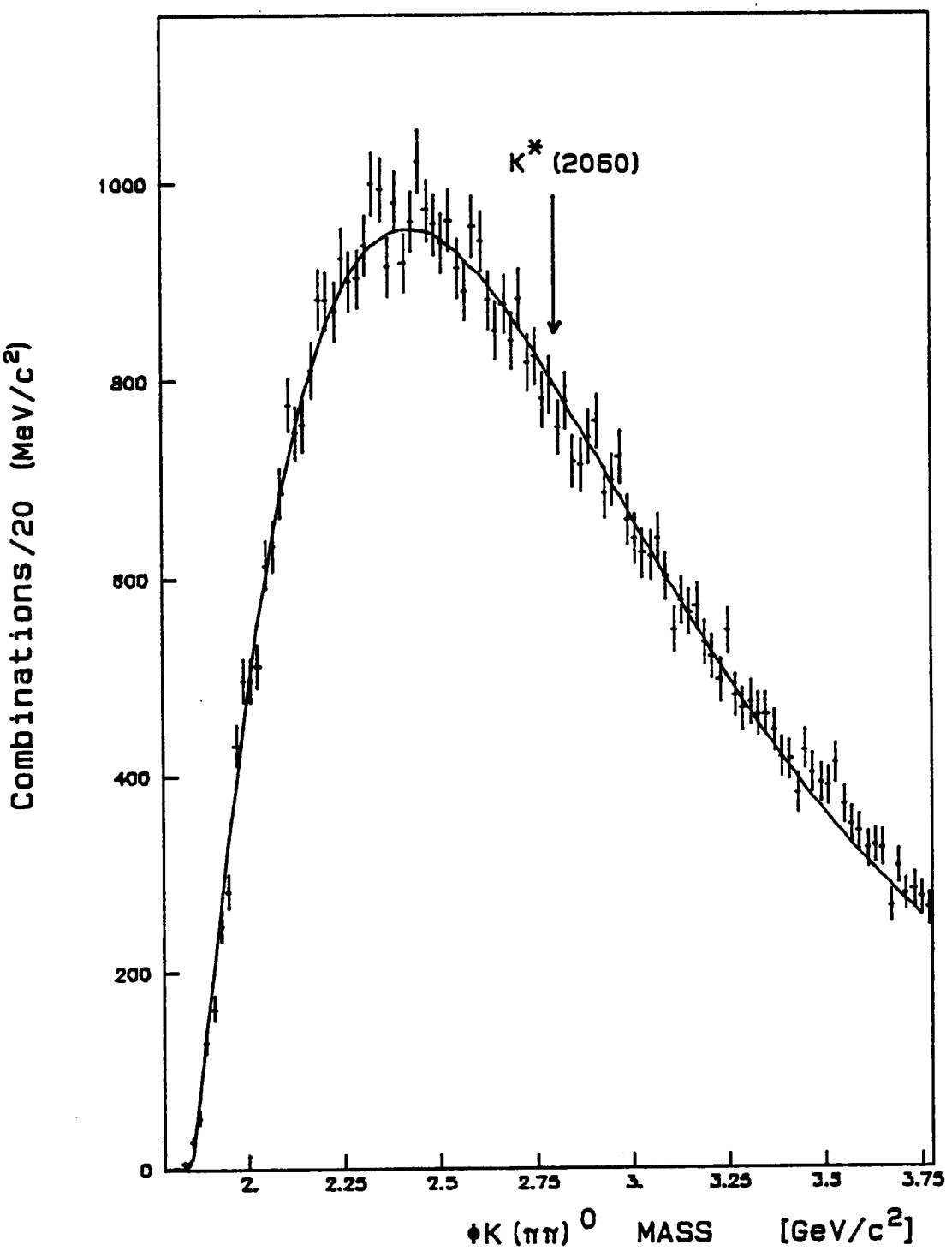

Fig. 5.3.3: The $\phi K^{\pm}(\pi\pi)^{0}$ mass spectrum.

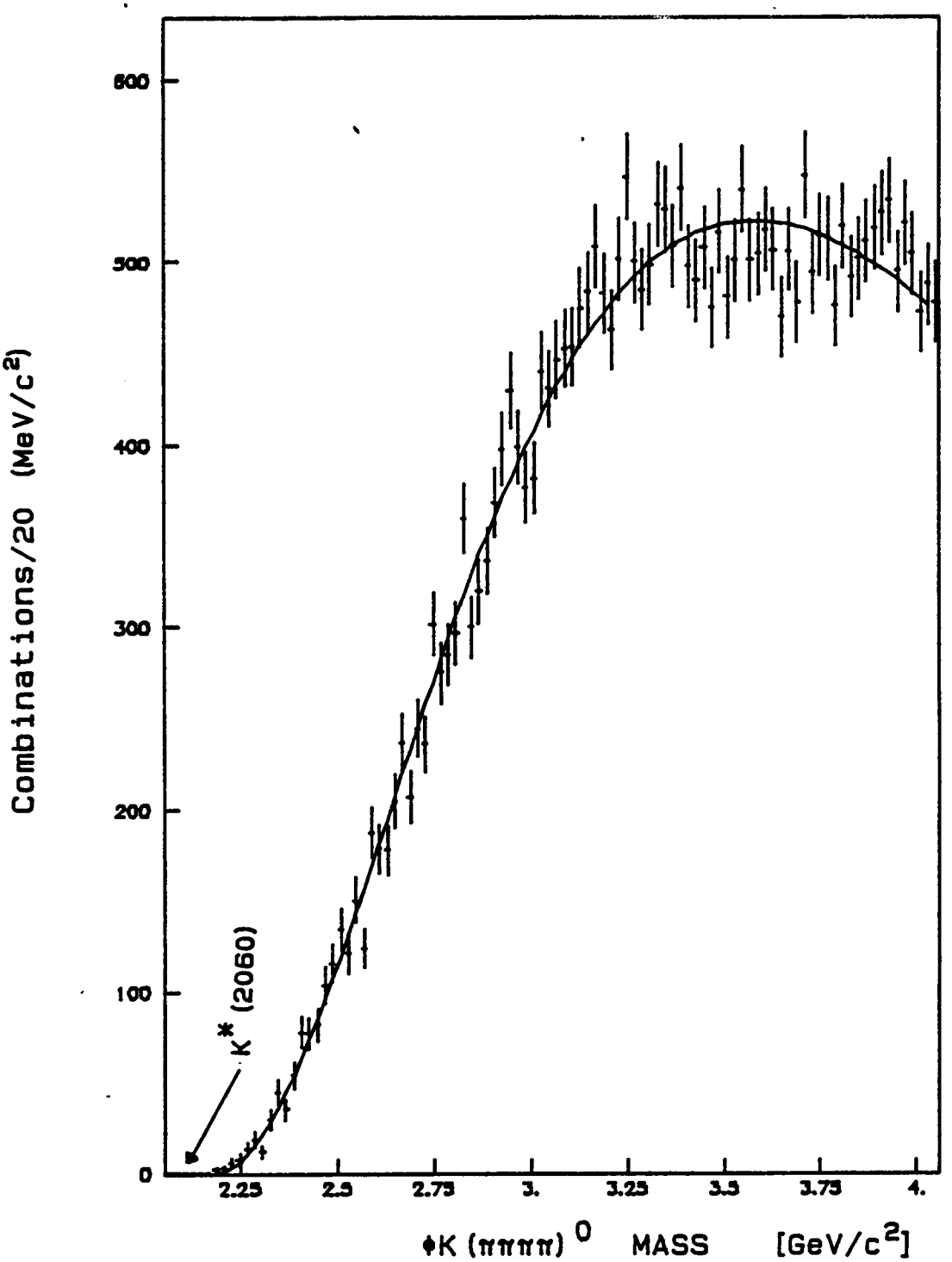

Fig. 5.3.4: The $\phi K^{\pm}(\pi\pi\pi\pi)^{0}$ mass spectrum.

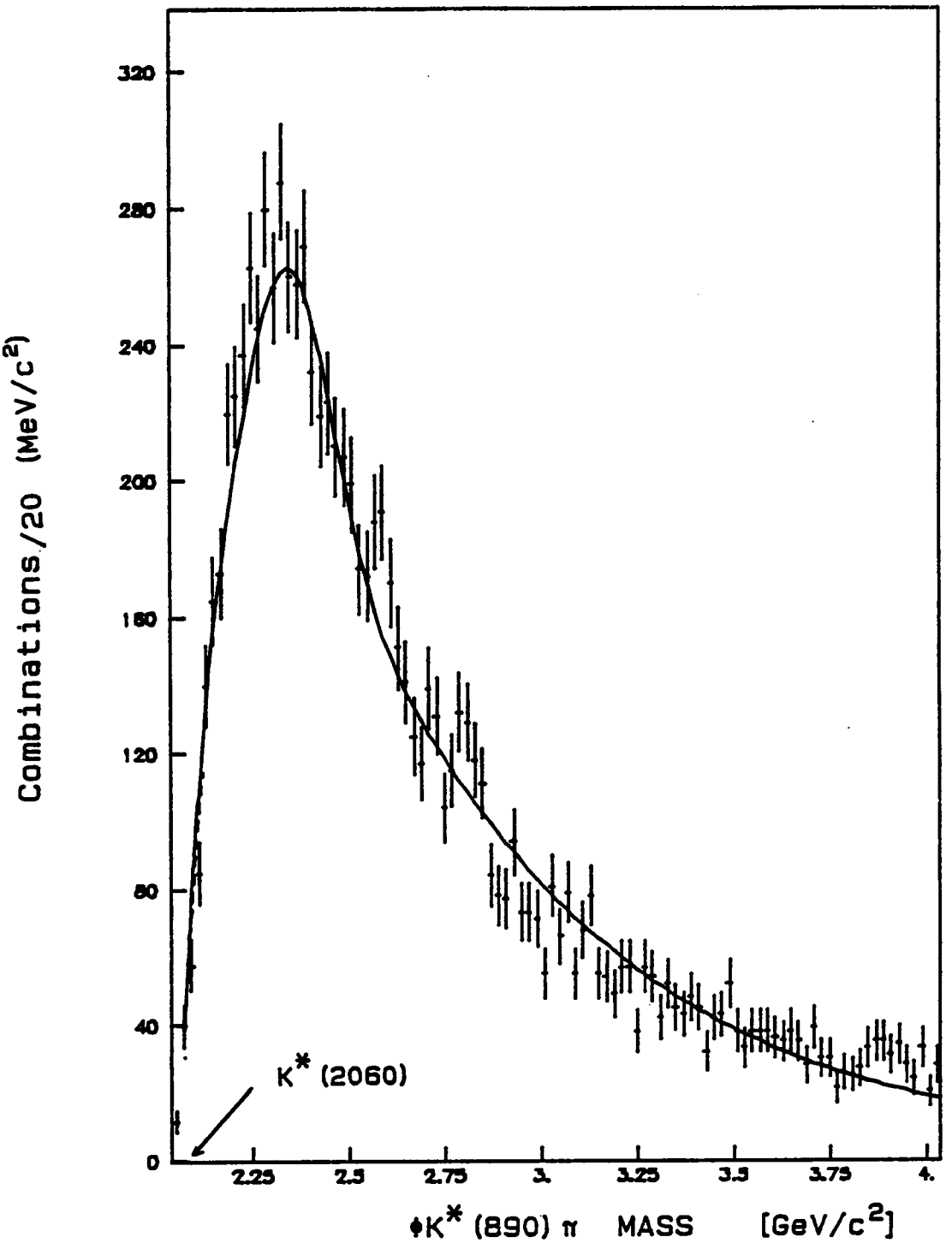

Fig. 5.3.5: The $\phi K^{0*}(890)\pi^{\pm}$ mass spectrum.

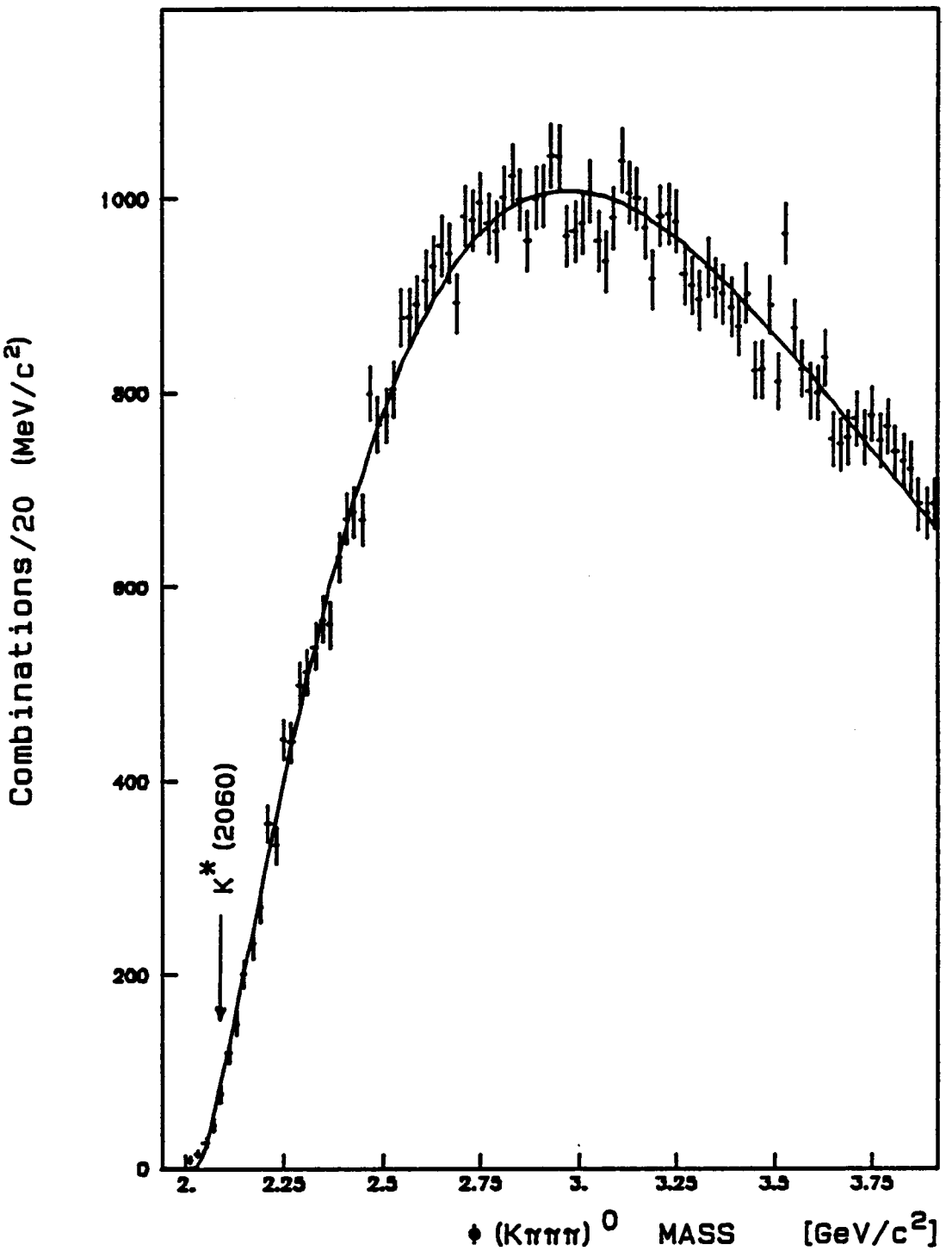

Fig. 5.3.6: The $\phi(K\pi\pi\pi)^0$ mass spectrum.

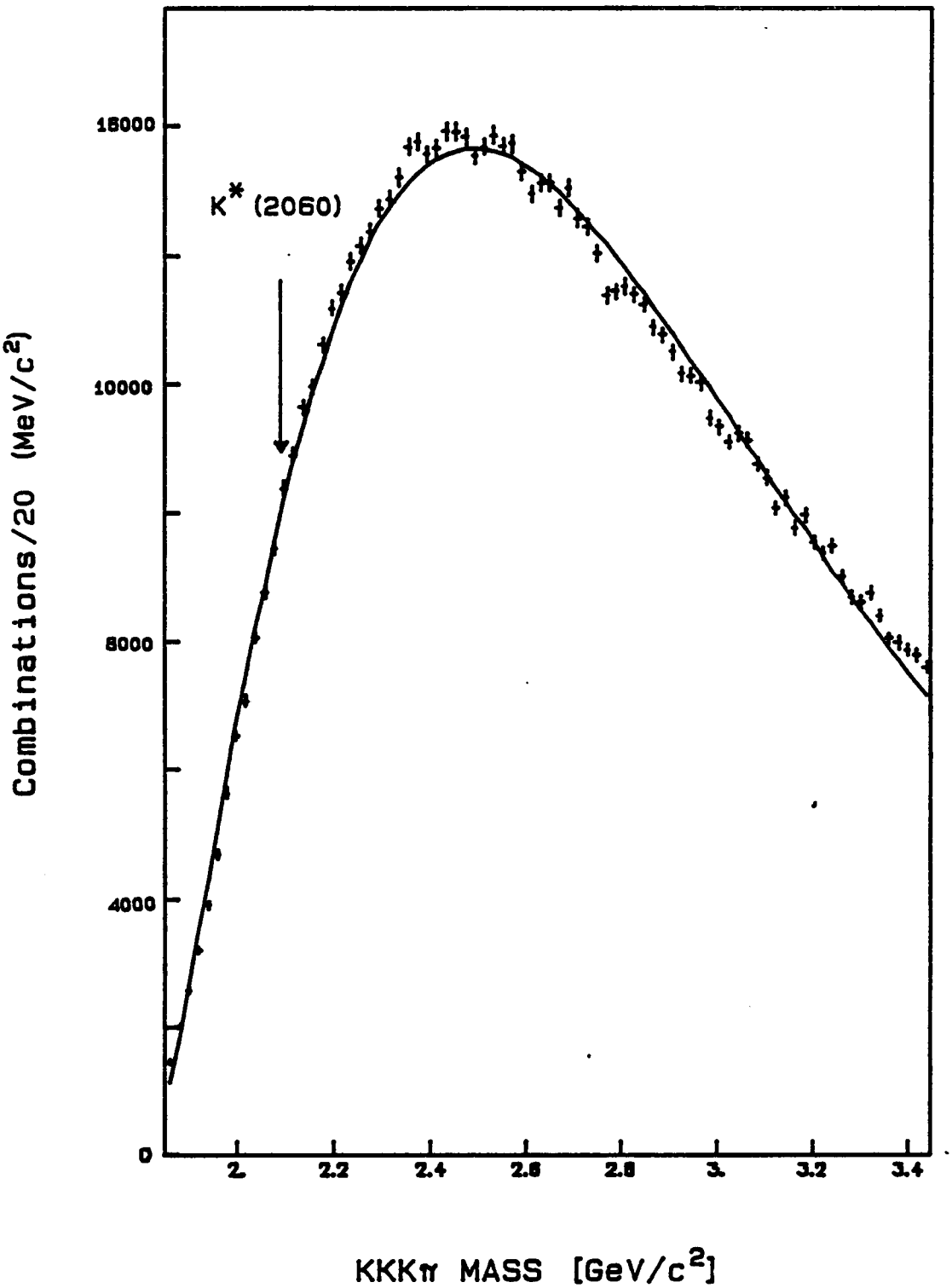

Fig. 5.3.7: The KKKπ mass spectrum.

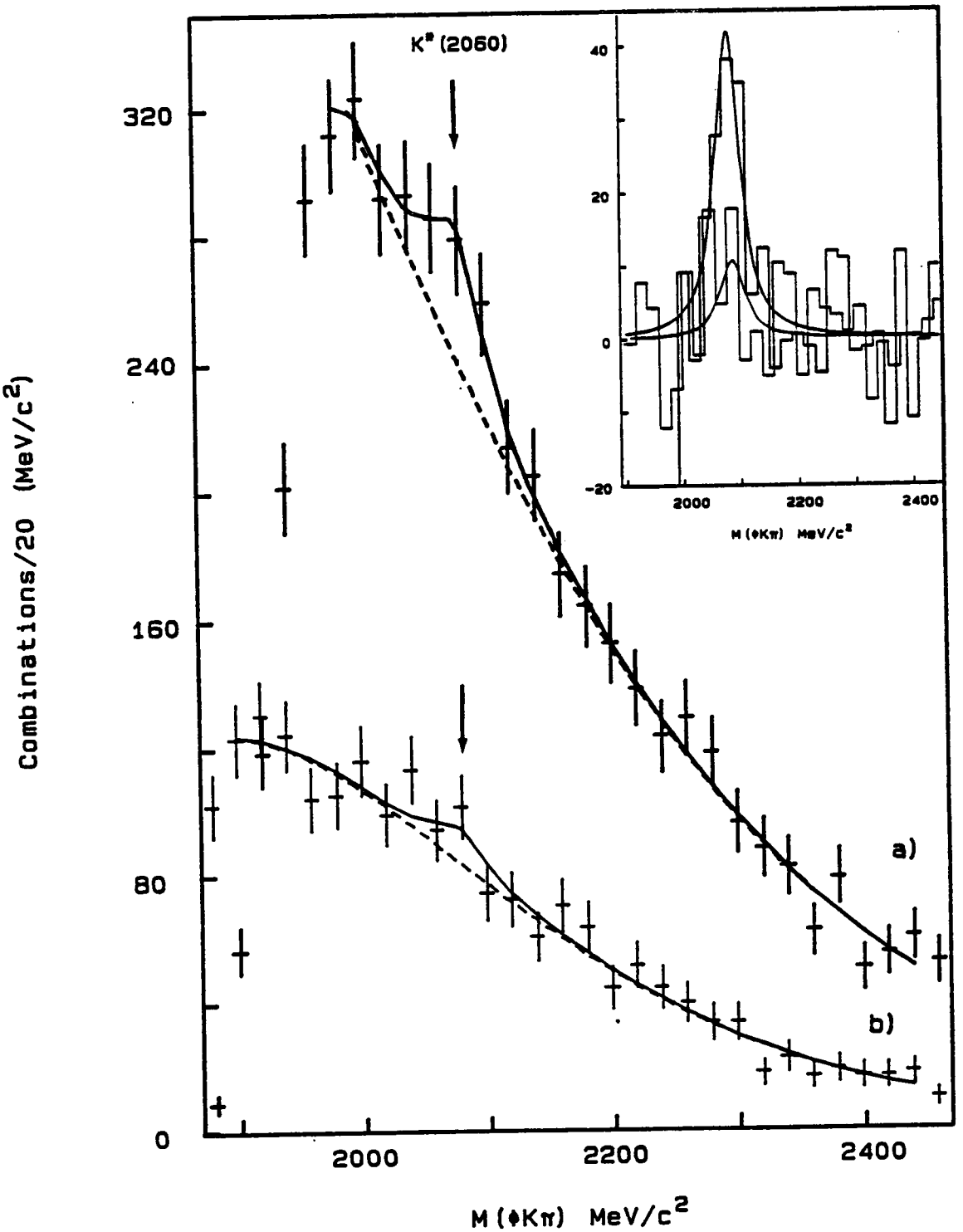

Fig. 5.3.8: The $\phi K\pi$ with $(K\pi)$ in $K^{0*}(890)$ (a) mass-band and (b) side-band.

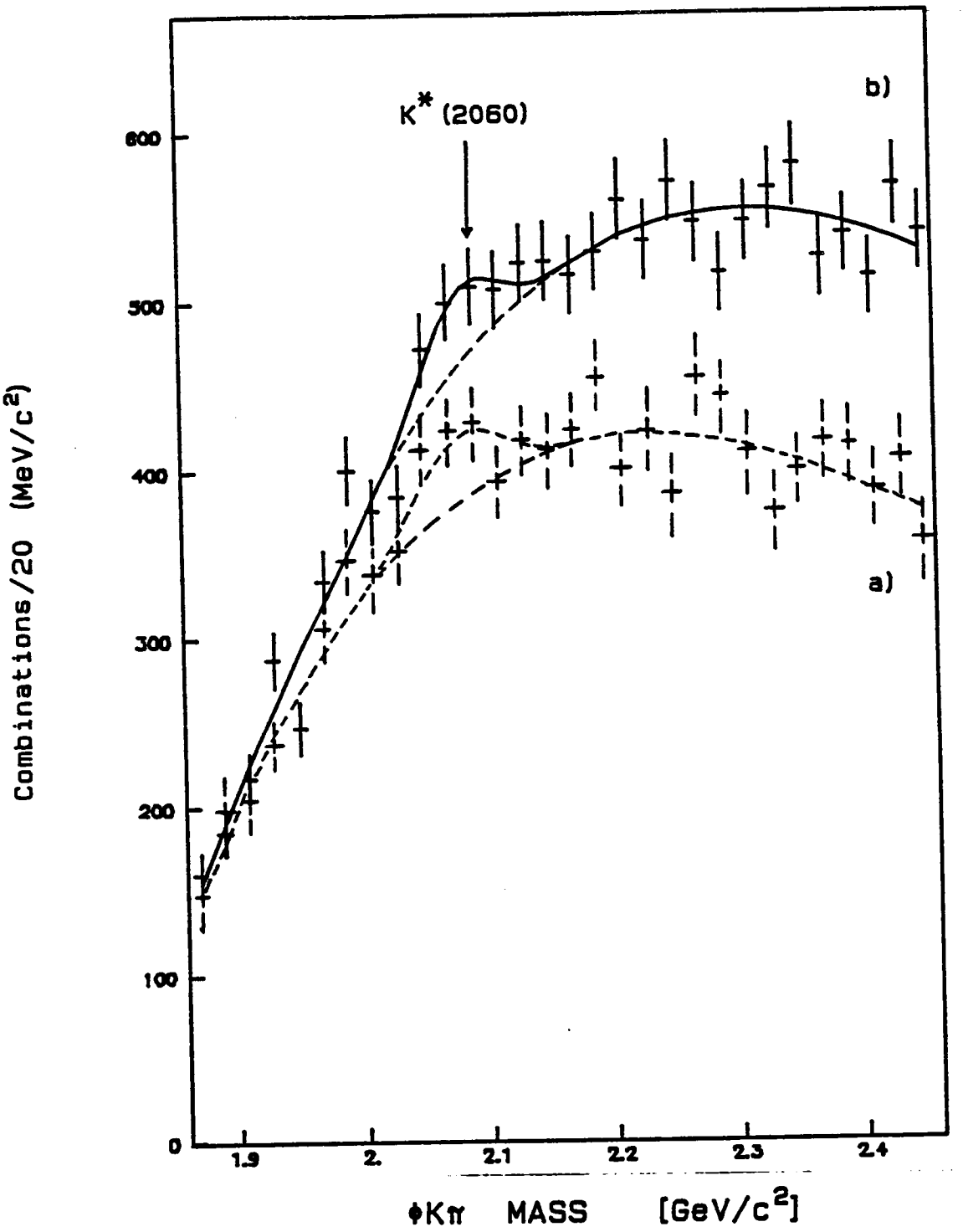

Fig. 5.3.9: Mass spectra for (a) $\phi K^+\pi^-$ and (b) $\phi K^-\pi^+$.

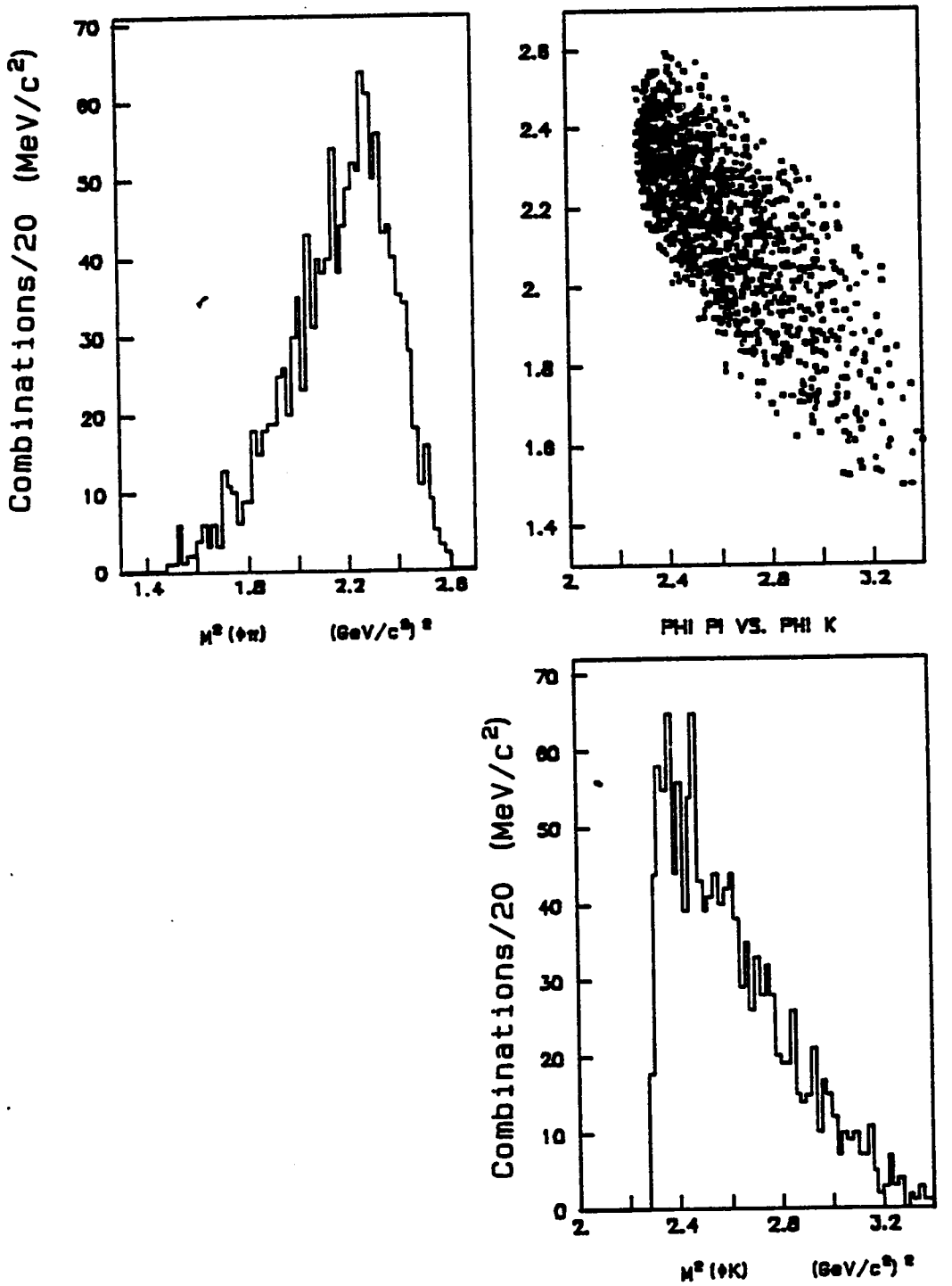

Fig. 5.3.10: The $\phi K\pi$ Dalitz plot.

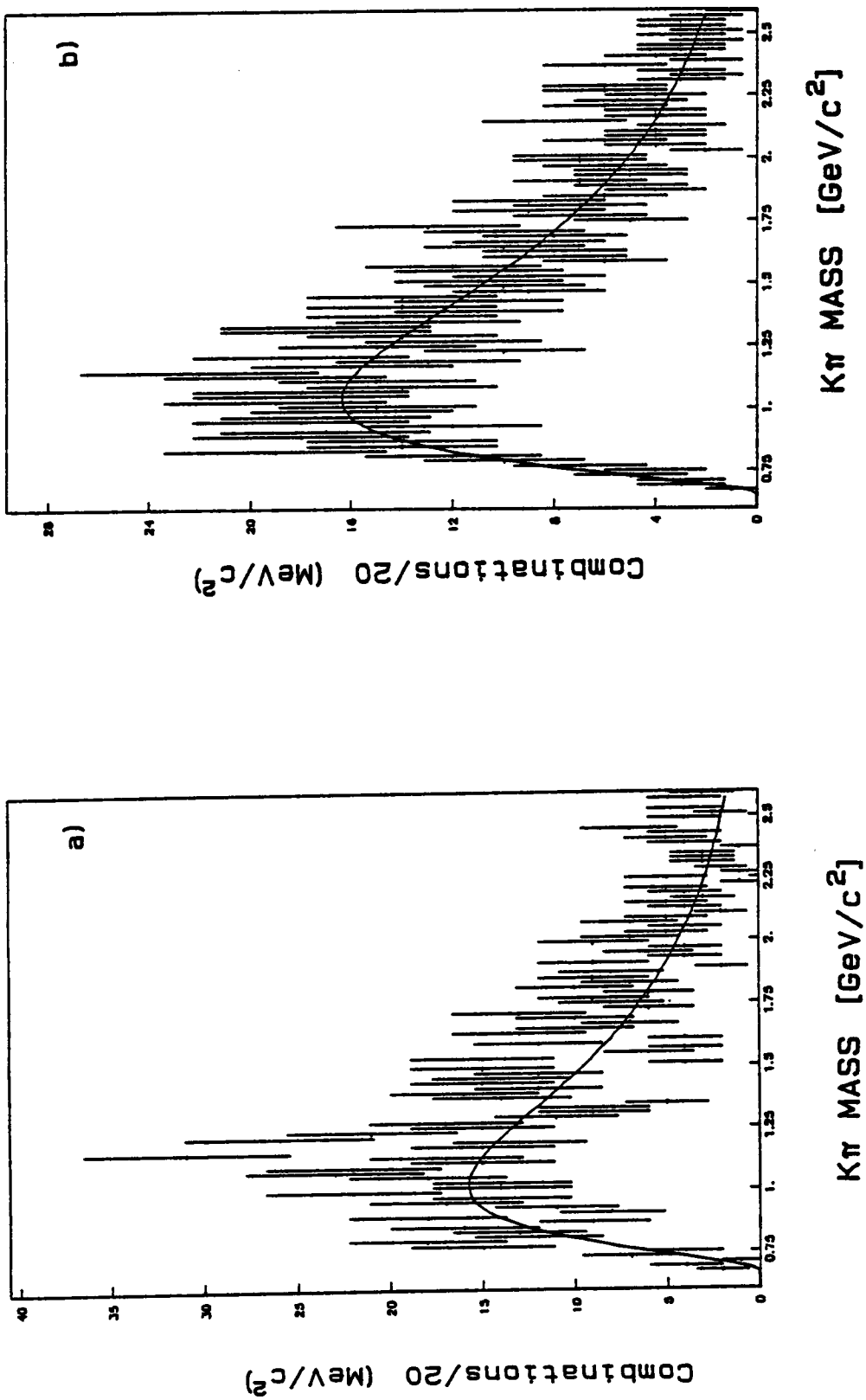

Fig. 5.4.1: The Kπ mass spectra for particles outside the K°*(2060)
(a) mass-band and (b) side-bands.

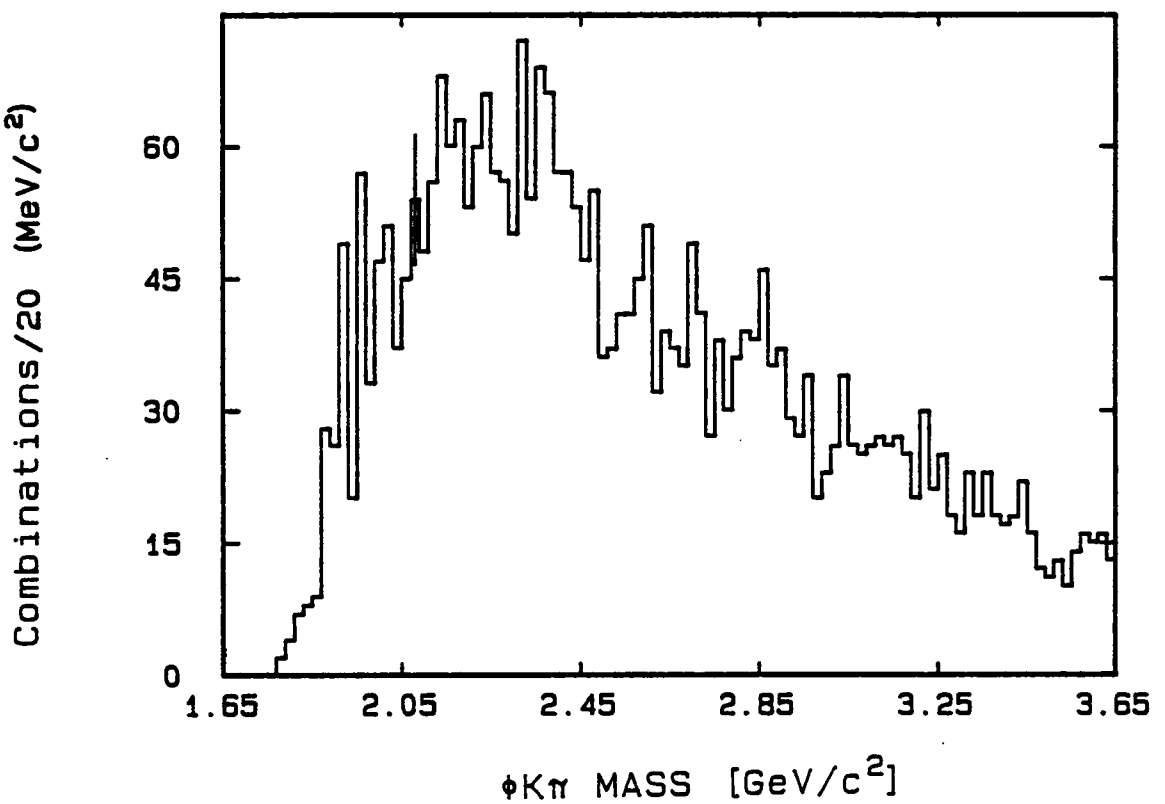

Fig. 5.4.2: The $\phi K\pi$ mass spectra for $pN \rightarrow (\phi K\pi)(K\pi(890))X$.

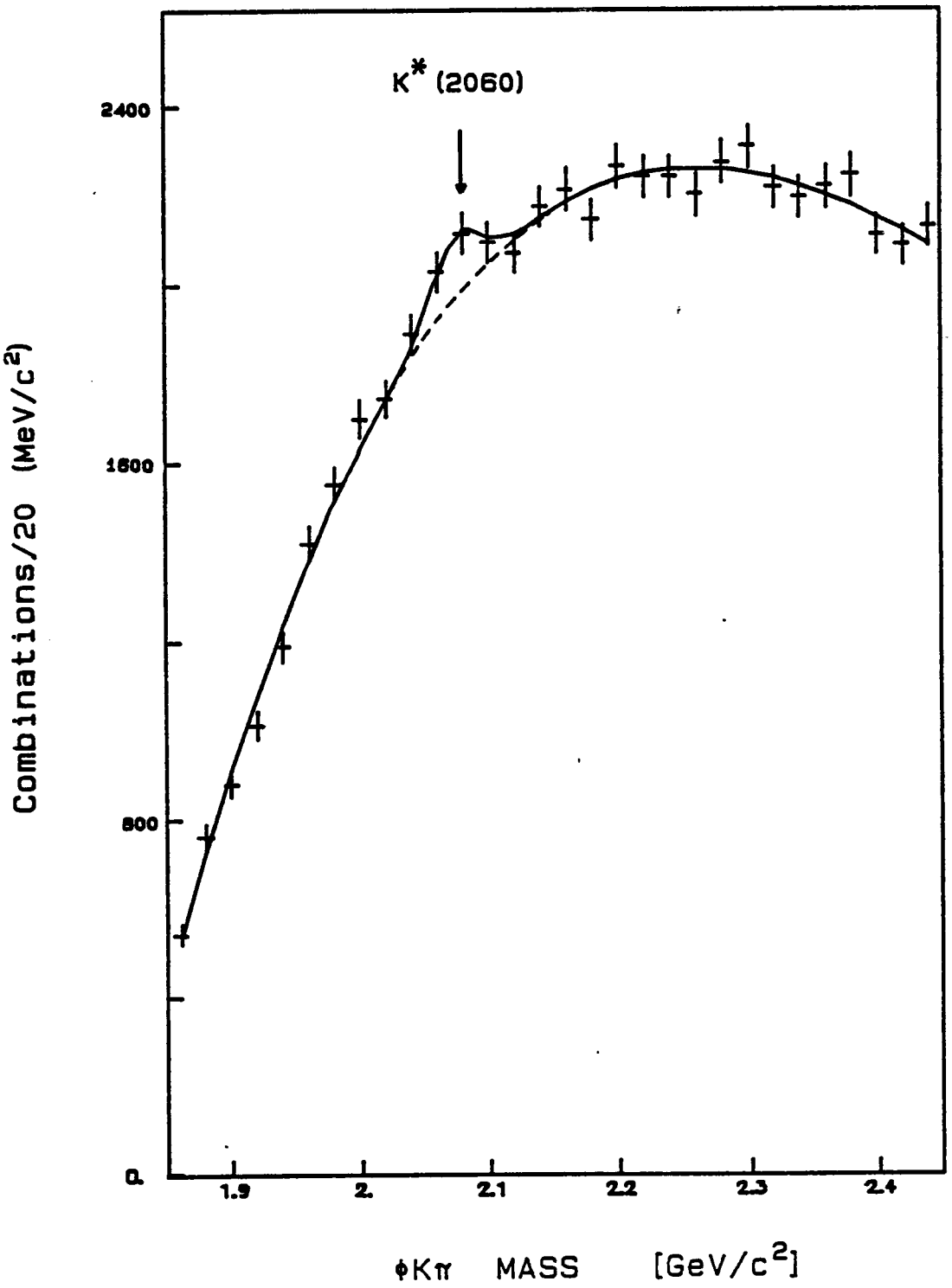

Fig. 5.4.3: The $\phi K\pi$ mass spectrum for the 3-K sample.

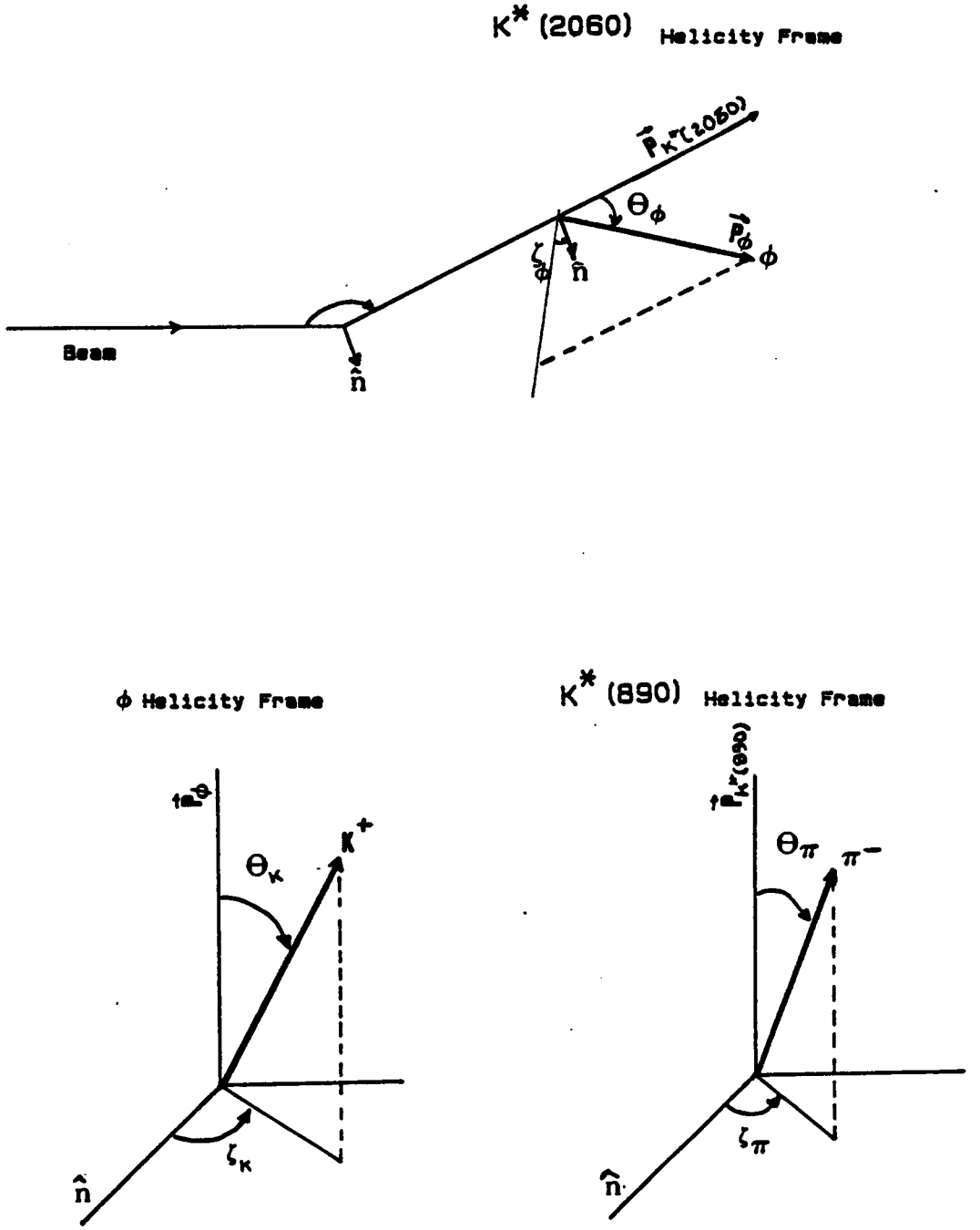

Fig. 5.5.1: The $K^{0*}(2060) \rightarrow \phi K^{0*}(890)$ decay angles definition.

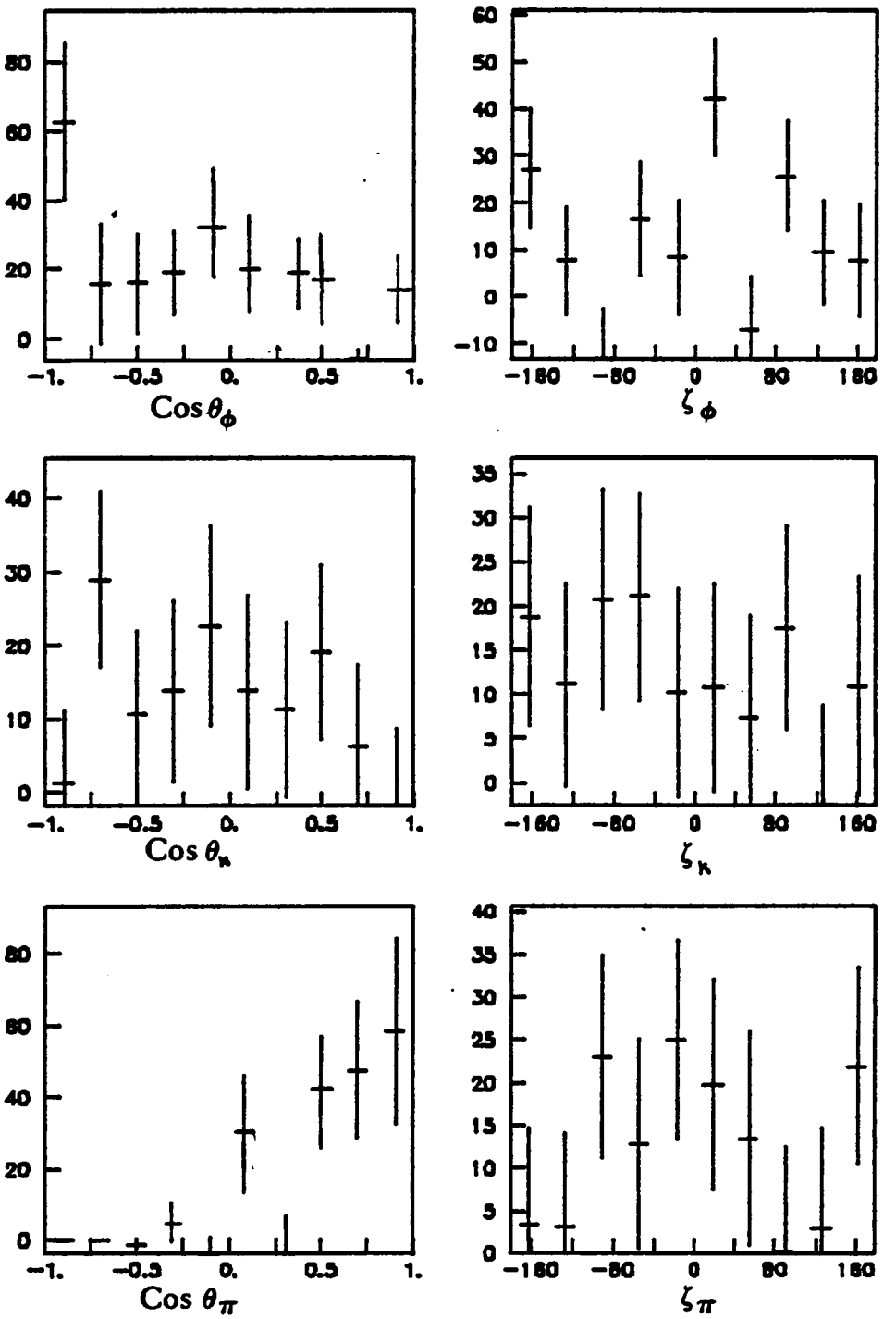

Fig. 5.5.2: The $K^{0*}(2060) \rightarrow \phi K^{0*}(890)$ angular distributions.

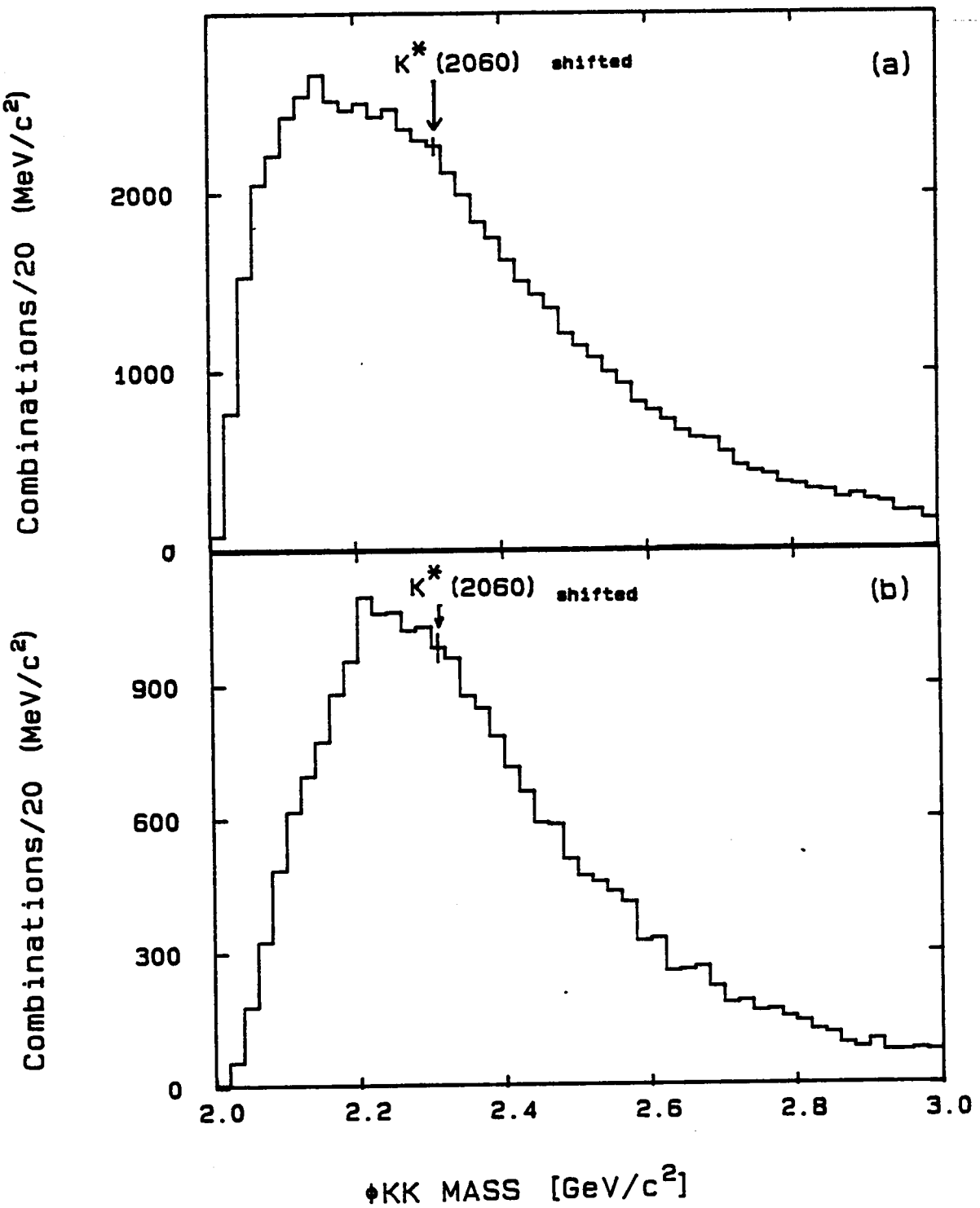

Fig. 5.6.1: The mass spectra of (a) ϕKK and (b) $\phi K\pi$ redefining the pion as a kaon.

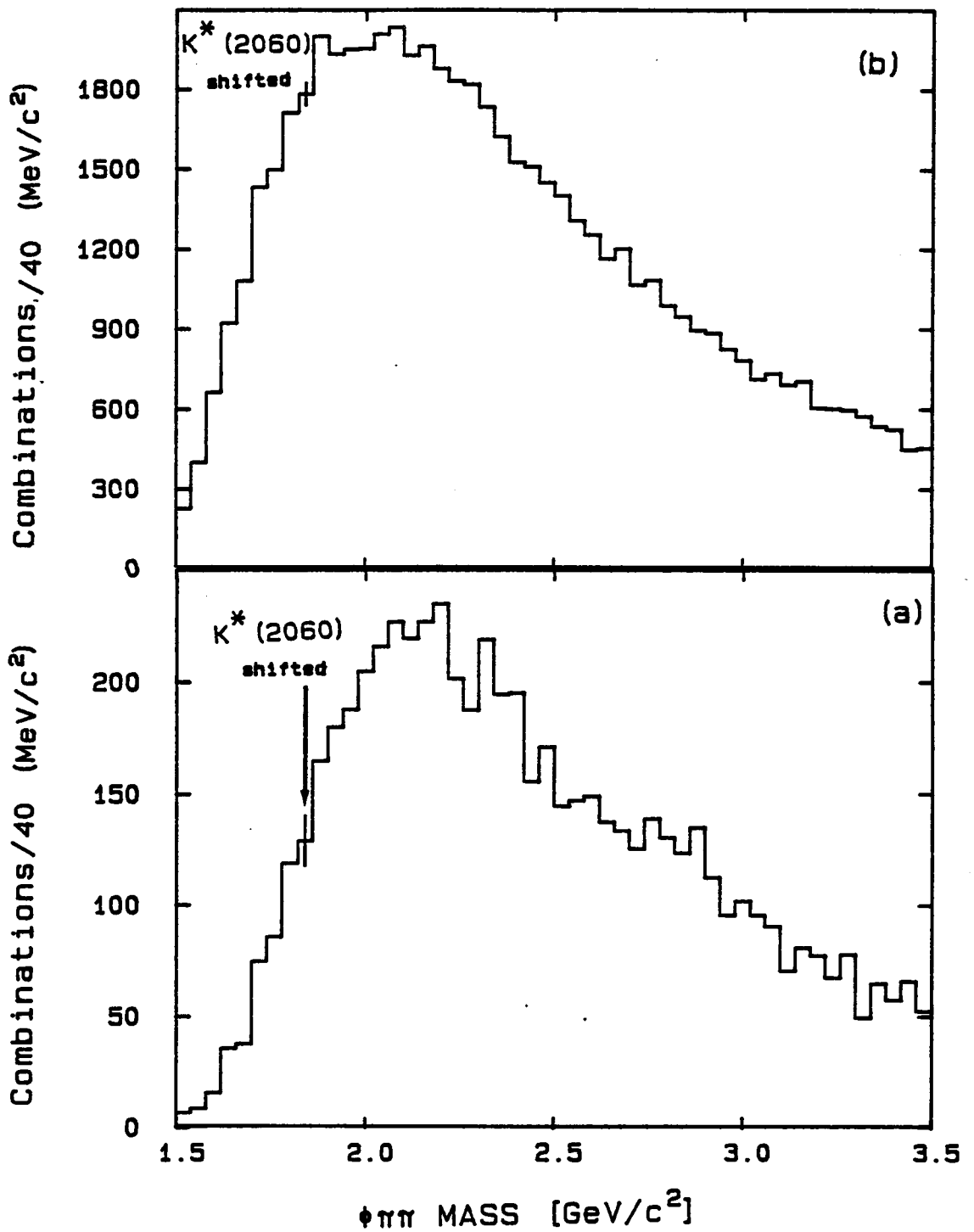

Fig. 5.6.2: The mass spectra of (a) $\phi\pi\pi$ and (b) $\phi K\pi$ redefining the kaon as a pion.

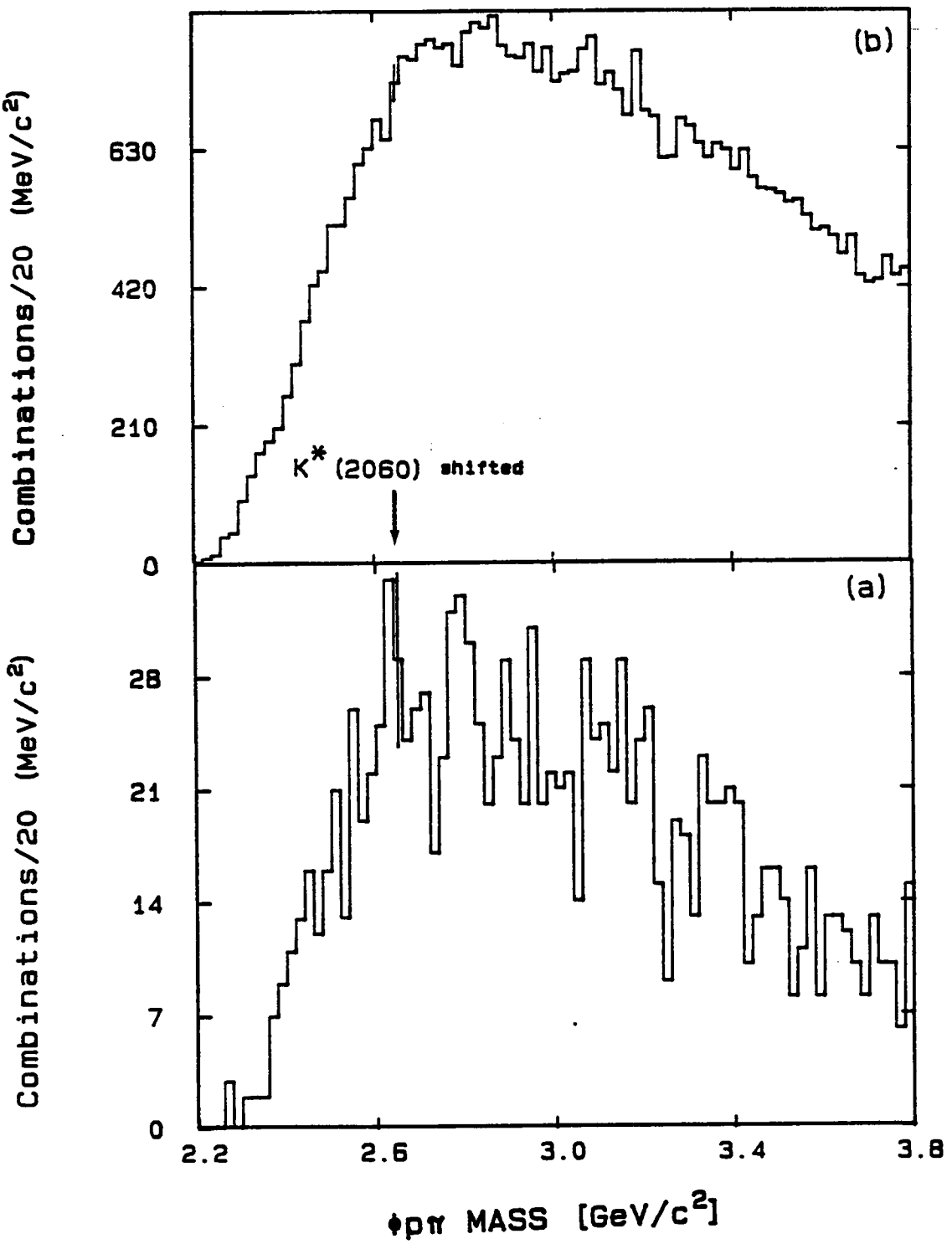

Fig. 5.6.3: The mass spectra of (a) $\phi p\pi$ and (b) $\phi K\pi$ defining the kaon as a proton.

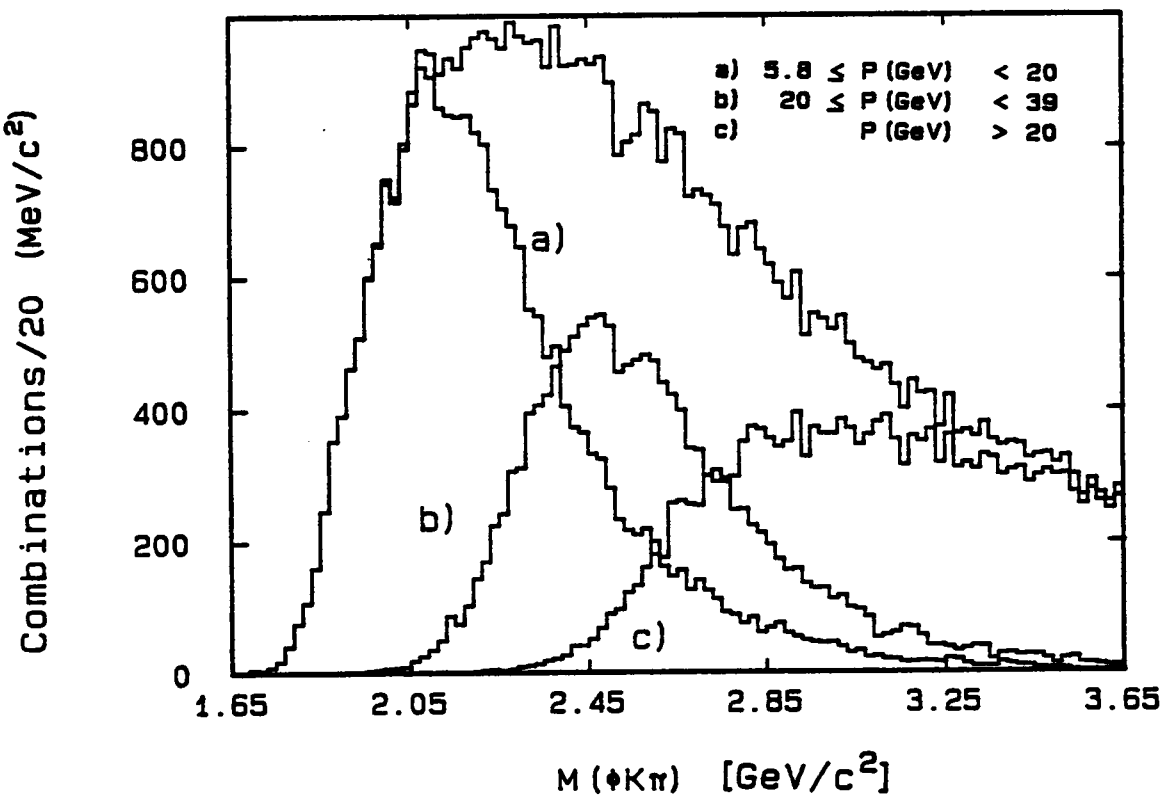

Fig. 5.6.4: The $\phi K\pi$ mass spectrum for pions from different momentum regions.

The three page vita has been removed from the scanned document. Page 1 of 3

The three page vita has been removed from the scanned document. Page 2 of 3

The three page vita has been removed from the scanned document. Page 3 of 3